Skoltech

Skolkovo Institute of Science and Technology

Proceedings of the Skoltech Energy PhD Seminar

2017/18

Skoltech

Skolkovo Institute of Science and Technology

Skoltech PhD Energy Seminar Proceedings 2017/2018

The Proceedings is a collection of the original research papers written by the participants of the second Skoltech PhD Energy Seminar in the 2017-2018 academic year.

The Skoltech PhD Energy Seminar unites students enrolled on Skoltech PhD Programs associated with the Centers of Electrochemical Energy Storage, Energy Systems, Hydrocarbon Recovery, and Photonics & Quantum Materials.

The Seminar promotes the exchange of knowledge, methodologies, and research questions across the fundamentally different scientific areas in accordance with the Skoltech vision of multidisciplinary research and education oriented to innovation. The main goal of the Seminar is to create and maintain interdisciplinary links between students doing research related to energy resources, generation, storage and distribution, as well as methods, models, devices and materials for efficient energy use.

Besides its immediate research-oriented goal, the pragmatic aim of the Seminar is to engage PhD students in professional academic communication activities based on the principles of ethics and peer review. During the Seminar, students were required to present the results of their research, write an article for the Proceedings according to a template, and peer review two papers submitted by the Seminar participants.

In preparation for the Proceedings, each paper was anonymously reviewed by two peers and checked by a language instructor. The final versions had to incorporate comments from the referees and editors to be accepted for the Proceedings.

Based on the experience of the previous year, the second Seminar was optimized in terms of the timeframe and the number of participants, which allowed us to pay more attention to the best writing, reviewing and research presentation practices. So we believe that the quality of papers accepted and published here in part compensates their modest number.

We appreciate the efforts and devotion of all the Seminar attendees and the contributions of their supervisors. We are grateful to the Skoltech Dean of Education Dr. Anna Derevnina for supporting the Seminar initiative. We also thank Mrs. Irina Velichko and Ms. Elena Barinova for preparing this document for publication.

Prof. Alexei Buchachenko (Seminar instructor)

Dr. Anna Sharova

Prof. Elizaveta Tikhomirova

CONTENTS

RESEARCH ARTICLES:

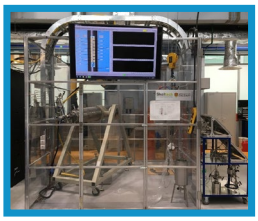

- Kerogen conversion into hydrocarbons led to the increase in sample porosity and permeability
- Valuable data for further numerical simulation were obtained
- Results indicated a high potential of high-pressure air injection for Bazhenov Formation

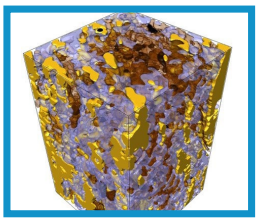

- Development of unconventional reservoirs requires new approaches and technical solutions
- Digital rock technology was used for the development of an integrated model of fracture propagation at nano- and micro-scales
- A complex of experimental methods was presented for filling digital rock model

- The proposed techno-economic analysis allows determining economic viability of energy storage systems (ESS) for installation in power system
- Optimal design of ESS was done with respect to optimal scheduling of all assets within the network
- To account for variability and repetitiveness of demand, the recursive clustering technique was applied to the historical demand data to derive five representative scenarios and the corresponding frequency of occurrence

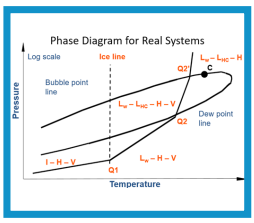

- Natural gas hydrate is considered an important substitute for fossil fuels in the twenty-first century
- The equilibrium dissociation conditions of simple hydrates of methane are investigated
- A new thermodynamic method is proposed that makes it possible to reveal the thermodynamic inconsistency of the experimental data and thereby ensure their correct smoothing and interpolation
- Smoothed data on three-phase equilibria of methane hydrate is obtained, which make it possible to calculate correctly the enthalpies of methane hydrate decomposition to ice and water and to estimate the hydrate number *n* at the quadrupole point

FOCUS:

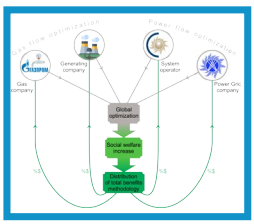

- Global optimization should be performed for a real case in order to estimate social welfare increase
- Methodology of total benefits distribution should be suggested
- Application of global dispatching and optimization needs significant technical and regulatory development
- Contingency analysis can be also performed for the coupled systems

Research Articles

Experimental Research of High-Pressure Air Injection in Bazhenov Shale

Tatiana Bondarenko

Abstract - Bazhenov oil shale contains high potential oil resources that can be unlocked through finding a suitable and efficient recovery technique. The aim of this study is to understand the kerogen thermal decomposition and oxidation mechanisms; to obtain the data needed for further numerical simulation; and to evaluate a high-pressure air injection (HPAI) potential to generate oil and gas from kerogen. This work includes laboratory investigation of kerogen oxidation process via thermal microscopy, high-pressure ramped temperature oxidation (HPRTO) experiment and combustion tube (CT) test. Thermal microscopy experiments showed that kerogen conversion into hydrocarbons during pyrolysis and oxidation led to the increase in sample porosity. In addition, intensive cracking was noticed at 450°C during the oxidation process, while cracking occurred through the formed voids. Temperature profiles, obtained in HPRTO experiment, identified the initial onset temperature of the kerogen oxidation (140°C) and maximum temperatures that the oxidation front. As a result of the CT test, the maximum temperature achieved was 463°C, while oil ignited readily at 200°C. The permeability of some samples reached 5.77 mD and the porosity increased up to 32%. CT test results indicated a high potential of HPAI recovery method for Bazhenov Formation.

Index Terms - high-pressure air injection, kerogen, Bazhenov Formation, thermal microscopy, high-pressure ramped temperature oxidation

I. Introduction

As world supplies of conventional crude oil continue to dwindle, interest in unconventional oil is growing. Oil shale contains a vast amount of immature organic matter, called kerogen, which is solid and not soluble in organic solvents. If we heat the rock, we can accelerate the natural maturation process to generate oil and gas. Oil shale contains high potential oil resources that can be unlocked through finding a suitable and efficient recovery technique. However, for Bazhenov Formation (BF), the major shale resource in Russia, the potential enhanced oil recovery (EOR) methods are not thoroughly investigated. Bazhenov Shale is Upper Jurassic – Lower Cretaceous clay-siliceous shales with carbonate admixture in the West Siberian Basin [1]. The thickness of the formation varies from 5÷10 to 20÷40 meters. Total organic carbon (TOC) of core samples varies from 2 to 18 wt.%, and consists primarily of amorphous kerogen. BF rock is characterized by very low porosity and permeability [2]. Therefore, the study of enhanced recovery methods for BF is important for the development of unconventional reserves.

Thermal EOR methods involving heating the rock to generate hydrocarbons from kerogen must be considered. One of the effective techniques might be high-pressure air injection (HPAI), which involves the oxidation front initiation that does not only move the oil by combustion gases, heated fluids and steam, but also causes the increase of reservoir pressure and temperature. It has been proved that the development of chemical reactions model and its kinetics is crucial for the success of air-injection-based processes [3], [4]. The classical heavy oil kinetic models consist of pyrolysis, oxygen addition reactions and bond scission reactions [5]. In case of oil shale, kerogen adds complexity to a chemical reaction model. Assessing the suitability of air-injection-based EOR is not a straightforward procedure in general, while assessing this method for such a complex system as oil shales is even more complicated. In order to make this process effective in Bazhenov oil shales, it is essential to understand the mechanism of kerogen conversion process. Kerogen is a cross-linked, high molecular weight solid substance with a complex structure. Moreover, the accurate chemical structure of kerogen is unknown. As a result, it has complicated behavior while heating. Therefore, a unique experimental

T. M. Bondarenko is with the Center for Hydrocarbon Recovery, Skolkovo Institute of Science and Technology, Skolkovo Innovation Center, Building 3, Moscow 143026, Russia (e-mail: tatiana.bondarenko@skoltech.ru).

research is required for the better understanding of kerogen thermal decomposition and oxidation mechanisms; obtaining the data needed for further numerical simulation; and evaluating an HPAI potential to generate oil and gas from kerogen.

Working on the experimental plan preparation, we design experiments that can help us answer the following questions:

- How much oil can we generate from kerogen in-situ?
- How do the reservoir properties change after implementing the technology?
- What unpredicted difficulties will we face during the pilot project?
- How can we develop and modify the chemical reactions and kinetics model in numerical simulation?

This work includes laboratory investigation of kerogen oxidation process via thermal microscopy, high-pressure ramped temperature oxidation experiment and combustion tube test.

II. Kerogen Thermal decomposition and oxidation mechanisms

Thermomicroscopy tests were conducted to study kerogen conversion, namely thermomicroscopy in an atmosphere of the air to study oxidation mechanism, and thermomicroscopy in an atmosphere of inert gas to study pyrolysis mechanism [6]. Carl Zeiss Axio Scope A1 microscope and a heating stage Linkam TS1500 were used to monitor changes in the morphology and the macrostructure of the BF sample while heating up to 720°C. The heating rate was 10°C/min and flow rate of the helium and air was 100 ml/min. In order to investigate conversion of kerogen visually during oxidation and pyrolysis, two thin rock sections of 5×5×1 mm were prepared. Video and photo reports, which showed the dynamics of changes in the void space, were obtained. Conversion of kerogen and rock mineral components during heating of the thin section of rock up to 720°C with helium and air purge was monitored.

A. Thermal microscopy: pyrolysis

Helium purge simulated pyrolysis process. Fig. 1 and 2 present images of a thin section before and after heating up to 720°C with helium purge. It can be noticed that dark black areas disappeared while heating. It probably can be explained by bitumen decomposition. Sizes of voids formed were determined in photos.

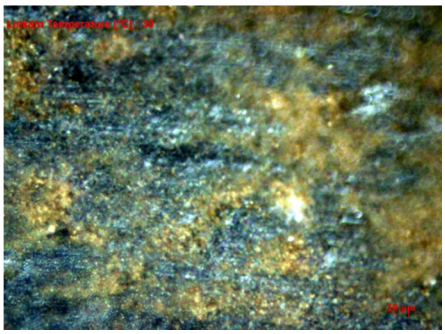

Fig. 1. Before heating. Microscope resolution is 20μm [6].

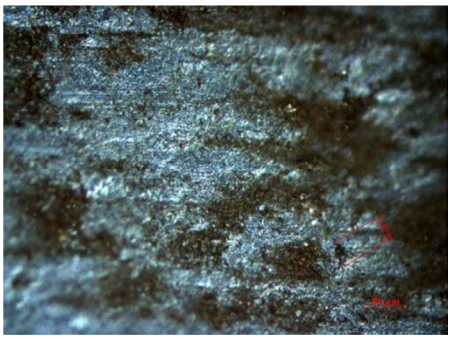

Fig. 2. After heating up to 720°C with helium purge. Microscope resolution is 50μm [6].

B. Thermal microscopy: oxidation

Air purge simulated oxidation processes. The high temperature reactions resulted in the decomposition of minerals in the samples (Fig. 3 and 4). The transformation of dark gray siliceous minerals into white burned minerals was detected at 540°C. Formation of magnetic minerals occurred due to the pyrite oxidation. Red minerals in Fig. 4 look like iron oxides.

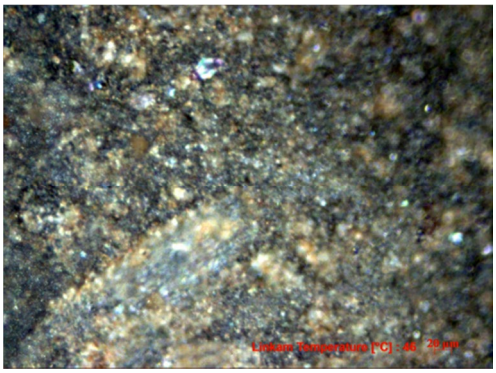

Fig. 3. Before heating up to 720°C with synthetic air purge. Microscope resolution is 20μm [6].

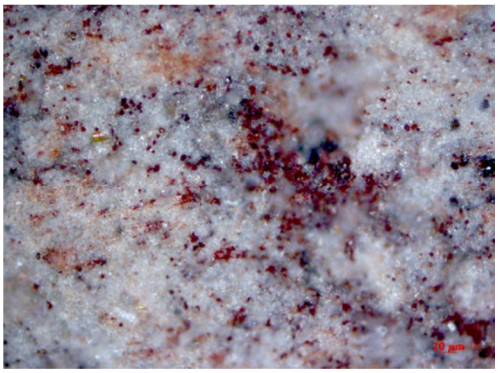

Fig. 4. After heating up to 720°C with synthetic air purge. Microscope resolution is 20μm [6].

Conversion of kerogen into hydrocarbons during oxidation caused the formation of pores, as can be seen in the images (Fig. 5). Organic matter solid monitored was 23.43 μm in diameter. During the oxidation of shale sample, intensive fracturing occurred at 450°C, as can be seen in Fig. 5. It should be pointed out that cracking occurred through voids (red circles in Fig. 5), formed due to organic matter oxidation process.

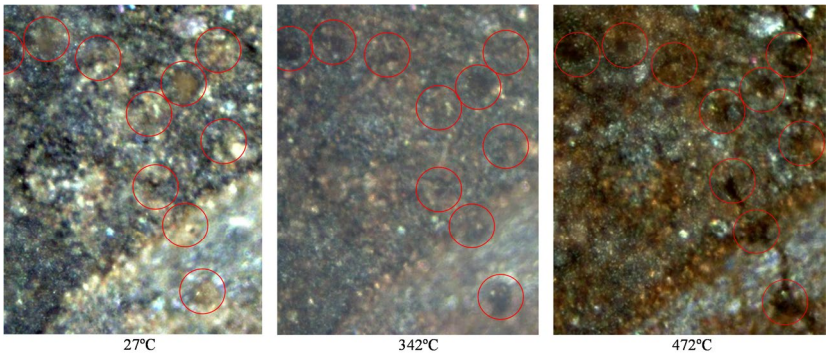

Fig. 5. Cracking of thin section during heating in the air [6].

III. High-pressure ramped temperature oxidation test

This test was conducted using the unique experimental equipment – HPRTO system [4]. It is the thin-walled type reactor with a pressure jacket. Pressure is carefully balanced between the inside and outside (the annular space between the pressure jacket and tube wall), while reactor pressure is maintained by means of a gas pressure controller at the outlet of the tube. Gas is injected top-down. Evolved gasses from the reactor are identified in gas chromatographs, while liquid samples are collected for further compositional analysis.

The aim of this test was to evaluate the potential of HPAI method in generating hydrocarbon gases and oil from kerogen using special experimental equipment [7]. The non-extracted crushed core was packed into a one-inch flow reactor, which was subjected to uniform heating at a rate of 40°C/h up to 500°C under reservoir pressure (28 MPa). During the tests, evolved gasses were constantly identified, and liquid samples were collected into four traps for further analysis. Temperatures of seven zones were measured by means of thermocouples, inserted into the reactor. Each zone was 57 mm in length.

As a result of this test, temperature profiles, gas compositions, volume and composition of generated/displaced fluids were obtained. Results of core post-analysis revealed that no kerogen remained in the core. Temperature profiles (Fig. 6) identified the start of kerogen oxidation (140°C) and maximum temperatures that can be reached during the exothermic processes of HPAI.

Initial reactions were reactions of low-temperature oxidation (LTO). This conclusion can be drawn from the increase of the nitrogen content in gas produced; oxygen was consumed without forming a sufficient amount of carbon oxides (Fig. 6). Most of the oxygen uptake occurred after the exothermic reaction in the second zone. It can be noted that kerogen and its thermal decomposition products burn more slowly than oil does. It is evident from the shape of the oxygen consumption curve and the exothermic peaks, appeared after 500°C. This may be due to the fact that the kerogen thermal decomposition occurs up to 650°C, so we steadily have new oxidative pyrolysis products that consume oxygen in the air. The high content of methane confirms the data obtained in [8], where constant heating was performed in closed reactors at different temperatures. According to the results of those tests, it was noted that after 480°C the main products were only coke and methane.

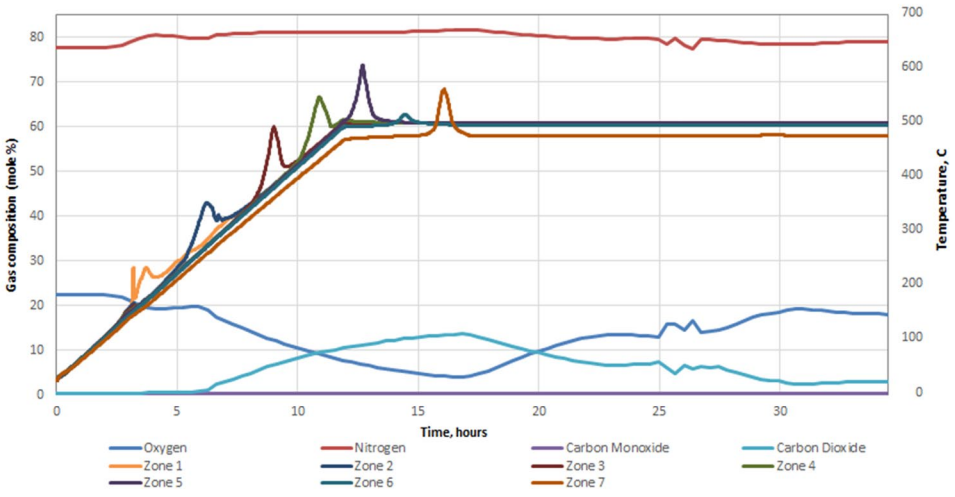

Fig. 6. Temperatures profiles and gas compositions (CO, CO_2, N_2, O_2). Gas chromatograph's delay time of 1.47 hours has been applied [7].

Based on the analysis of the masses of the fluid, generated as a result of oxidation reactions and reactions of thermal decomposition of kerogen, 25.1 g of water-oil emulsion (where around 80 wt.% was water) and 0.99 g of hydrocarbon gases were generated from the 92 cm^3 of rock (14.79 g of hydrocarbons).

Future work should include numerical simulation of experimental tests to adjust chemical reactions and kinetics. The implementation of the experimental work has made it possible to substantially reduce the uncertainties revealed in oil shale oxidation and pyrolysis behavior.

IV. Combustion tube test

A laboratory experiment in CT was carried out to evaluate the potential of the HPAI and to determine combustion parameters in the Bazhenov source rocks [9]. Core pack consisted of rock samples of various shapes from several oil fields. It was saturated with dead oil from the selected wells in BF (Fig. 7). The ignition zone of CT was preheated to 200°C. After that oil ignited readily. During the process, evolved gases were monitored to assess the oxidation reactions intensity and obtain a gas composition. Produced oil samples were collected and analyzed. Pyrolysis analysis of the crushed core was conducted prior to and after the thermal and chemical exposure. As a result, several exothermic peaks in each section of the CT were noticed, which may correspond to the oxidation of the initial oil, synthetic oil, and kerogen. Due to the combustion front propagation, the total residual oil saturation was around 2%. Minimal residual oil saturation was observed in zones behind the combustion front, maximum residual oil saturation was observed ahead of the combustion front. It should be noted that kerogen conversion was detected in zones ahead of the front. The maximum temperature that was reached was 463°C. CT results suggested high potential of HPAI for the development of BF.

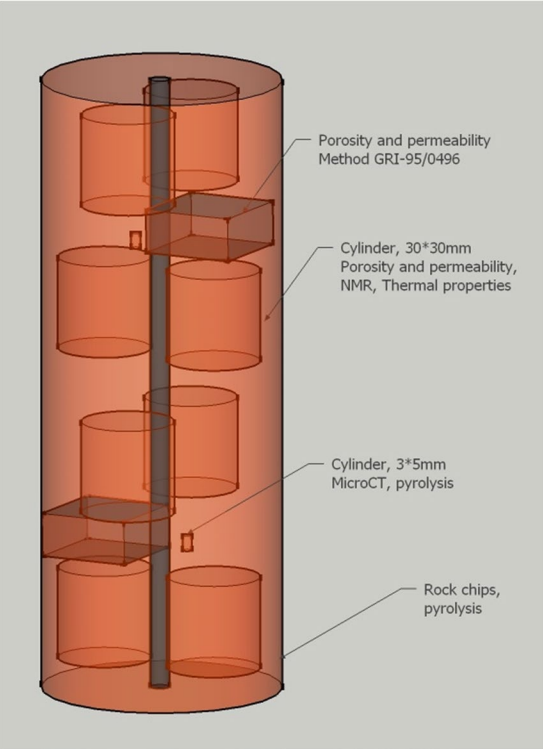

Fig. 7. Schematics of combustion tube packing.

In order to analyze changes in properties of rocks under the thermal and chemical exposure in CT test, a number of supplementary studies of rock samples were performed [10]. A series of experiments included: measurements of permeability and porosity of the cylindrical core samples to evaluate changes in reservoir properties due to the processes occurred in CT; a study of cylindrical samples in nuclear magnetic resonance (NMR) relaxometer to obtain two saturation profiles along the samples before and after the experiment in the CT; measurements of thermal conductivity for assessing their changes as a result of the oxidation front propagation through the cylindrical samples.

Rock properties, such as porosity and permeability, were significantly enhanced by the oxidation front propagation, while the permeability increased up to 5.77 mD, and some samples porosity reached 32%. The results of the thermal properties measurements showed hydrocarbons oxidation and displacement. The thermal conductivity of samples decreased due to the fact that air with its low thermal conductivity filled the cracks formed. Due to the intensive cracking of the samples, the anisotropy of samples thermal conductivity increased. By studying the saturation profiles one can evaluate the progress of the oxidation front propagation in the samples. The decrease of NMR porosity indicated the kerogen conversion.

V. Conclusions

1. Thermal microscopy experiments showed that kerogen conversion into hydrocarbons during pyrolysis and oxidation led to the increase in sample porosity. In addition, intensive cracking was noticed at 450°C during the oxidation process, while cracking occurred through the formed voids.
2. Temperature profiles, obtained in HPRTO experiment, identified the initial onset temperature of the kerogen oxidation (140°C) and maximum temperatures at the oxidation front.
3. The maximum temperature that was reached in CT test was 463°C, while oil ignited readily at 200°C.
4. The permeability of some samples reached 5.77 mD and the porosity increased up to 32%.
5. CT test results indicated a high potential of HPAI recovery method for BF.

VI. References

[1] N. S. Balushkina, G. A Kalmykov, R. A. Khamidullin, V. S. Belokhin, N. I. Korobova, N. N. Petrakova, and A. I. Bakay, "Complex lithophysical typization of Bazhenov Formation rocks from core analysis and well logging," SPE Russ. oil gas Explor. Prod. Tech. Conf. Moscow, 2014. DOI: 10.2118/171168-MS.

[2] R. A. Khamidullin, G. A. Kalmykov, D. V Korost, N. S. Balushkina, and A. I. Bakay, "SPE 162094 Reservoir properties of the Bazhenov formation," 2012.

[3] D. Gutierrez, R. G. Moore, M. G. Ursenbach, and S. A. Mehta, "The ABCs of In-Situ Combustion Simulations: From Laboratory Experiments to the Field Scale," Can. Unconv. Resour. Conf., 2011.

[4] R. G. Moore, S. A. Mehta, and M. G. Ursenbach, "A Guide to High Pressure Air Injection (HPAI) Based Oil Recovery," SPE/DOE Improv. Oil Recover. Symp., no. SPE 75207, pp. 1–7, 2002.

[5] P. S. Sarathi, "in Situ-Combustion Handbook - Principles and Practices," p. 424, 1999.

[6] T. Bondarenko et al., "Experimental investigation of thermal decomposition of Bazhenov formation kerogen: Mechanism and application for thermal enhanced oil recovery," J. Pet. Sci. Eng., vol. 150, no. December 2016, pp. 288–296, 2017.

[7] T. Bondarenko, L. Khakimova, A. Cheremisin, and M. Spasennykh, "SPE-187849-MS High-Pressure Air Injection Laboratory and Numerical Modelling in Bazhenov Source Rocks Key aspects of building an HPAI model , sensitivity analysis," 2017.

[8] T. Bondarenko, E. Popov, A. Cheremisin, I. Karpov, and N. Morozov, "Experimental assessment of the hydrocarbons yeilds from Bazhenov shale formation by kerogen conversion in the presence of supercritical water," Int. Symp. Soc. Core Anal., pp. 1–6, 2016.

[9] T.M. Bondarenko, E.Yu. Popov, A.N. Cheremisin, E.V. Kozlova, I.A. Karpov, N.V. Morozov, 2017. "Laboratory Modeling of High-pressure Air Injection in Oil Fields of Bazhenov Formation" (In Russ.). Neftyanoe khozyaystvo = Oil Industry 3: 34–39, 2017.

[10] T.M. Bondarenko, A.Z. Mukhametdinova, E.Yu. Popov, A.N. Cheremisin, A.G. Kalmykov, I.A. Karpov. "Analysis of changes in Bazhenov formation rock properties as a result of high-pressure air injection based on laboratory modelling data" (In Russ.), Neftyanoe khozyaystvo = Oil Industry, 2017, no. 3, pp. 40–44.

The First Step to Solving Geomechanical Problems with Digital Rock Technology: Experimental Part

Victor A. Nachev*, Andrey V. Kazak

Abstract - This article describes an approach to building a digital model of rock for the development of unconventional oil and gas reservoirs. The approach is based on digital rock technology. We solve the problem of fracture propagation in rock samples at nano- and microscale and utilize a set of experimental results to determine the mineralogical and chemical composition of investigated samples, its structure and mechanical properties. The technology takes into account natural uncertainties arising during experimental investigations of rock samples. As a result, experimental data for the construction of structural, mineral and mechanical digital models of target rock samples are obtained and processed. Recommendations for further research in this direction are provided in the conclusions.

Index Terms - digital rock, scanning electron microscopy, mechanical rock testing, multiscale, tomography, uncertainty analysis, unconventional reservoirs

I. Nomenclature

AFM	Atomic Force Microscopy
BTS	Brazilian Tensile Strength test
BSE	Back-Scattered Electron
CT	Computed Tomography
DEM	Discrete Element Modeling
DIC	Digital Image Correlation
DRP	Digital Rock Physics
DTS	Direct Tensile Strength test
EDS	Energy Dispersive Spectrometry
FEM	Finite Element Model
FFT	Fast-Fourier Transform
FIB-SEM	Focus Ion Beam – Scanning Electron Microscopy
QEMSCAN	Quantitative Evaluation of Minerals by SCANning Electron Microscopy
RP	Reservoir Properties
XRD	X-ray Diffraction

II. Introduction

Production of gaseous and liquid hydrocarbons from unconventional reservoirs is an important part of modern oil and gas industry. Engineers deal with various reservoir properties (RP) of such reservoirs that are

Victor A. Nachev is with the Center of Hydrocarbon Recovery, Skolkovo Institute of Science and Technology, Skolkovo Innovation Center, Building 3, Moscow 143026, Russia (e-mail: victor.nachev@skolkovotech.ru).
Andrey V. Kazak is with the Center of Hydrocarbon Recovery, Skolkovo Institute of Science and Technology, Skolkovo Innovation Center, Building 3, Moscow 143026, Russia.

determined by pore structure of rocks. In unconventional reservoirs pores and fractures in rocks exist on scales from centimeters to nanometers. Very small pores lead to the extremely low permeability of reservoirs. It means that due to relatively small fluid drainage zone inflow of hydrocarbons to the well will be low. To increase the efficiency of inflow, the drainage zone should be extended. This requires the application of near-wellbore stimulation, such as hydraulic fracturing.

Laboratory experiments of hydraulic fracturing operation on rock scale allow predicting parameters of hydraulic fracture propagation to some extent on the reservoir scale.

Traditional methods of rock exploration do not allow a complete evaluation of fracture distribution anisotropy, i.e., real capacity of the void space and microstructural features at different scales. For qualitative and quantitative estimation of RP, microstructures and compositions of rock samples, novel methods are required which will take into account high degree of heterogeneity of samples and provide high accuracy and reliability of results. One of the methods that takes into account microscale can be digital rock technology based on the mathematical processing of rock tomography at the microscale (micro-CT).

The technology of digital rock with laboratory experiments allows effective separation of rock lithological (lithotypes) and flow units in a studied rock sample, determining the structure of pore space and measuring its properties with calculation methods based on the density-functional method applied to multiphase hydrodynamics [1], [2]. Digital rock is converted in an unstructured mesh; general properties of the identified materials are laid in nodes of the mesh, and the solution is carried out in a geometry similar to the real structure of rocks [1]. Another effective method is upscaling of mechanical and physical properties of digital rock technology that allows propagating physical processes of sample scale model to reservoir scale model.

Digital rock physics has been actively studied during the last years. For simulating complex mechanical behavior such as rock failure, the discrete particle modeling approach is used [3]. Curves were simulated for axial stresses vs volumetric strains and for axial P- and S-wave velocities vs axial strain for three different sandstones: Castlegate, Obernkirchener and Saltwash South. Then these curves were obtained from laboratory experiments and compared with the simulated curves. Triaxial tests were with confining pressures 2, 7 and 15 MPa. As a result, the agreement of simulated and experimental data was rather good for strength parameters and for elastic stiffness and the discrete element modeling (DEM) approach appeared simpler and rather realistic.

Inverse digital rock physics (DRP) modeling approach was used for prediction reservoir parameters of digital cores [4]. This approach was based on an improved Lagrange interpolation algorithm to fit the calculation equation of elastic parameters of digital cores. As a result, the direct relations between reservoir and elastic parameters were applied.

When dealing with a digital rock, it is necessary to take into account the current reservoir simulation software and their capabilities. Comparative analysis of different algorithms and boundary conditions for DRP modeling was done [5]. The results for elasticity and electrical conductivity of S2, Berea, Fontainebleau sandstones, Finney pack and C1 and C2 carbonate were compared for Simpleware Physics Modules, Comsol Multiphysics and NIST codes. As a result, between Simpleware and Comsol there is a good agreement with a difference about 1% for effective elastic properties and 5% for conductivity. Simpleware is better for processing a large number of digital samples, Comsol is preferred for research purposes.

DRP technology is used to improve calibration of empirical and theoretical rock physics models if direct measurements of rock samples are absent. In particular, the influence of stress and strain loading conditions on elastic properties of digital rocks was investigated [6]. The five digital rocks with their computed tomography (CT), X-ray diffraction (XRD) analyses and thin sections from the Berea, Fontainebleau and Castlegate formation were studied. To compute effective elastic moduli, three numerical approaches were used: the dynamic pulse propagation method, the static finite elements method and the static fast-Fourier transform (FFT) method. As a result, laboratory experimental rock stiffnesses are consistently softer that what computed numerically, and strain loading conditions lead to stiffer results than using the stress boundary conditions for FFT method. Also, the elastic properties of carbonate rock samples were estimated using three-dimensional (3D) CT images based on Finite Element Method (FEM) and DEM in [7]. As a result, simulated data of bulk and shear modulus based on FEM were more similar to lab measurements than based on DEM.

DRP is used to compute petrophysical parameters (porosity, elastic modulus, etc.) from 3D multi-scale CT images and Back-scattered Electron (BSE) images [8]. Carbonate rock sample was studied in that work. Micro-CT images (39.48 μm/vx and 1.0357 μm/vx) are used as a large-scale porosity map, Nano-CT (65 nm/vx) – to compute petrophysical properties. As a result, after comparison estimated parameters from CT images and laboratory measurements the relative errors of a bulk modulus were ~77%, of a shear modulus were ~88%. The P- and S-wave velocities in carbonate rock samples were simulated based on CT images with 40, 4, 2, 1 and 0.5 μm/vx in [9]. As a result, after laboratory measurements, the relative errors with simulated results were 23.78% and 56.8% for P- and S-wave velocity respectively for the first carbonate sample and 54.39% and 62.43% – for the second. Also, P- and S-wave velocities in Berea sandstone were studied in [10]. As a result, the relative error of the calculated to measured data is about 4% for both velocities.

This article presents methods for studying fracture propagation at micro- and nano-scale using DRP technology.

III. Methods

The general workflow for the understanding of pore-scale reservoir model and its behavior for the optimal technology development of hydrocarbon reservoirs consists of three parts. The first part is building a broad self-consistent dataset containing petrophysical, geomechanical, rock structural and digital imaging data. It includes laboratory tests, microstructural study and data analysis. The second part is preparation and initialization of multiscale 2D and 3D digital rock models that is a transitional stage. It converts the multiscale model to FEM representation for building meshing. The third part is geomechanical numerical simulations of multiscale digital rock models on nano-, micro- and mesoscale separately that lead to the most probable realizations of fracture propagations in rock samples. A special focus has been set on accurate estimation of uncertainties [11].

The main methods utilized to construct multiscale digital rock models are presented below.

A. Computed Tomography

This method of X-ray tomography allows solving a huge number of geological problems, such as imaging of void space (cracks, cavities, pores), calculation of porosity, studying rock heterogeneity, allocation of various rock voids and inclusions, etc. Examples of using CT, sample preparations and CT equipment settings are presented in many contemporary publications, for example [1] and [12]. Typical resolutions for CT are from 0.5 to 50 μm/vx.

B. FIB-SEM

This method is used to determine coordinates of structural elements and it is used in addition to methods of CT. FIB-SEM investigations are carried out on a prepared surface of a rock sample. The roughness of the sample surface plays a primary role in generation of 2D and 3D maps with a spatial resolution of from units to 100 nm/px. The example of using FIB-SEM technology is presented in [13].

C. QEMSCAN

The method is based on SEM-scanning of coordinate points on the pre-defined grid on the sample surface. At each coordinate point the system determines the mineralogical composition based on the electron backscatter intensity. The chemical composition is determined by the secondary X-ray emission arising from the interaction of an electron beam with a mineral. Two-dimensional digital mineralogical and textural maps of rocks are obtained as a result of this method. Typical resolution for QEMSCAN is 1 mm. The mineralogy technology by FEI's QEMSCAN system is presented in [14].

D. Energy-Dispersive Spectroscopy

This method is used to study the microstructure of the void space and its mineral composition.

A substantiated decision on a study of representative zones of a rock sample for FIB-SEM using QEMSCAN and EDS methods analysis was made in the article [15]. Typical resolutions for EDS are units of μm.

E. Atomic Force Microscopy

This method is used for measuring elastic moduli of organic matter of rock samples. The method allows building a quantitative nano-mechanical map of minerals on the surface of the rock sample [16]. Typical resolution for AFM is 1 μm.

F. Direct and Brasilian Tensile Strength Test, Pseudo-Triaxial Compressive Strength Tests

These methods allow studying elastic and strength properties of rock samples. Standard methods are used to obtain elastic modules: ASTM D2936-08 [17] for DTS, ASTM D3967-05 [18] for indirect tensile strength test (BTS) and GOST 28985-91 [19] for pseudo-triaxial compression strength test.

G. Digital Image Correlation

This optical method is used for the measurement of deformations and displacement fields. The principle of DIC's work is in splitting the sample image into sectors and further analysis of movement on surface in each elementary window. The maximum correlation corresponds to the movement of the surface and gives the length and direction of the vector for each elementary window. The DIC tool allows determining locations and amplitudes of maximum strains that is very important in material testing. Also, it is used in an investigation of fracture mechanics in materials. Typical resolutions for DIC are from nm to m. The example of using DIC technology is presented in [20].

IV. Results

The first part of the general workflow is building a broad self-consistent dataset containing petrophysical, geomechanical, rock structural and digital imaging data.

Fig. 1 presents results of the Brazilian tensile strength (BTS) test and the pseudo-triaxial compression strength test. Red color means the first fractures in samples and green is for the second fractures. Yellow color is for the biggest minerals with volume more than 0.005 cm^3, blue highlights the biggest voids with volume more than 0.001 cm^3.

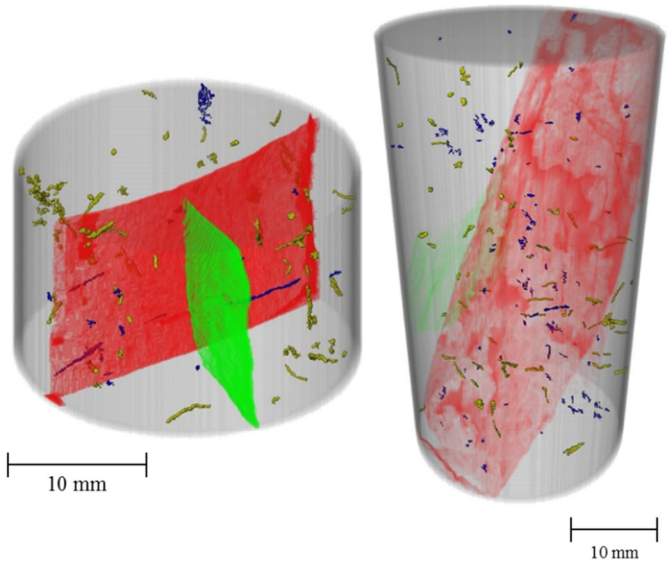

Fig. 1. CT of rock samples after tests with fractures: left – for BTS, right – for pseudo-triaxial compressive strength test [21].

Fig. 2 shows the density model (left) that presents the distribution of mineral phases and void elements in the studied rock sample. The distribution of all voids is presented in Fig. 2 (right) and is allocated by 3D image processing methods.

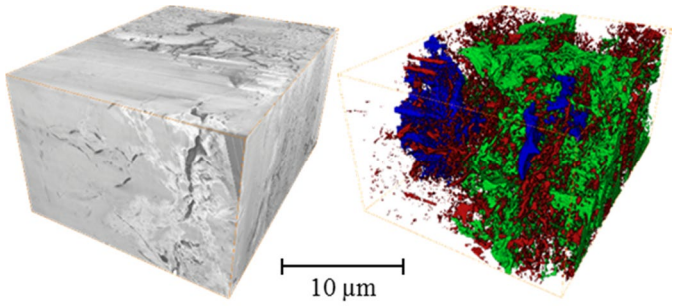

Fig. 2. 3D structure of voids after FIB-SEM investigations [21].

Fig. 3 presents mineral maps obtained by the automated mineralogy method QEMSCAN on the surface of the studied sample

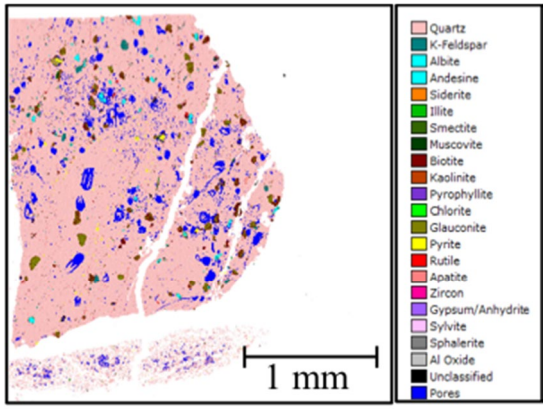

Fig. 3. 2D mineral map obtained with QEMSCAN [21].

Fig. 4 (left) presents the image of the surface of rock cut. Fig. 4 (right) shows the superposition of mineral composition maps on the image of the surface of rock cut.

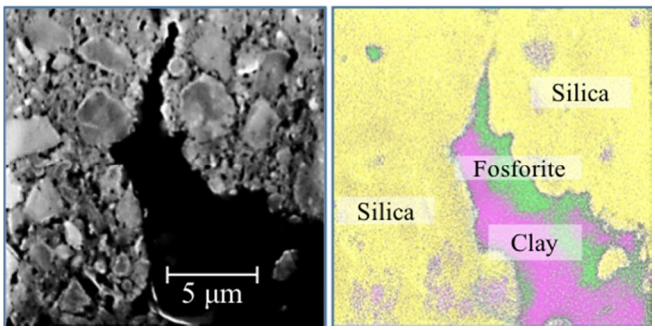

Fig. 4. 2D chemical map obtained with EDS [21].

Fig. 5 presents the loading and strain curves obtained in BTS test. Curves (solid lines) are drawn together with their total errors (pale background).

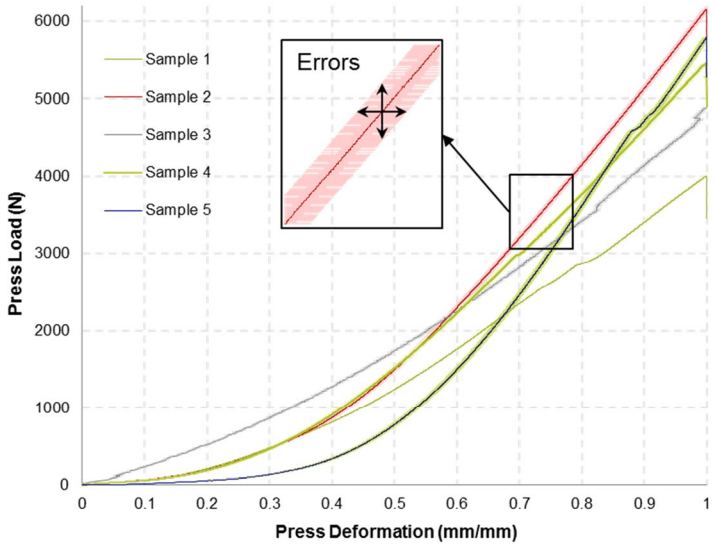

Fig. 5. Obtained mechanical properties of investigated rocks with BTS [21].

Fig. 6 presents DIC results of displacement fields during BTS test. The initial state of the sample is on the left part, before fracturing state – in the central part, after fracturing state – on the right part.

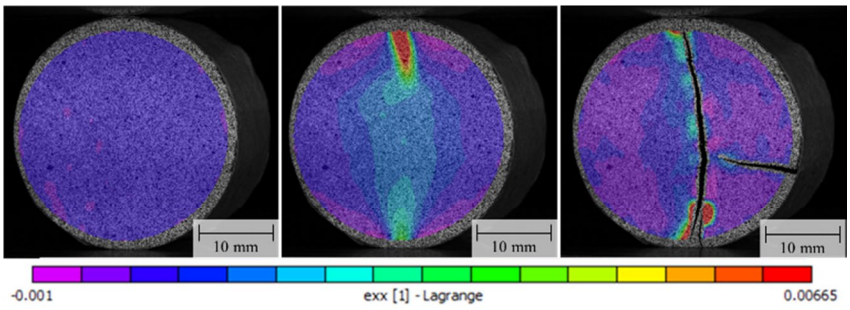

Fig. 6. Displacement field obtained with DIC [21].

Fig. 7 presents mechanical properties of sample's elastic moduli. On the left part of the figure red color is Young's modulus, black color – axial deformation modulus, on the right part red color – Poisson's ratio, black color – lateral deformation ratio.

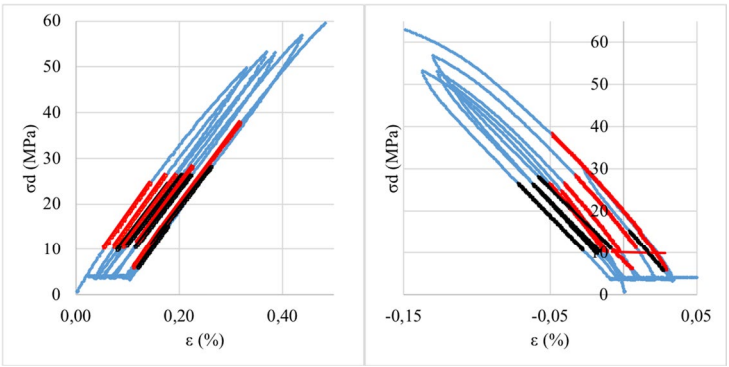

Fig. 7. Mechanical properties obtained with pseudo-triaxial compression strength test.

Fig. 8 presents Mohr circle plot for studied sample obtained in the pseudo-triaxial compressive strength test.

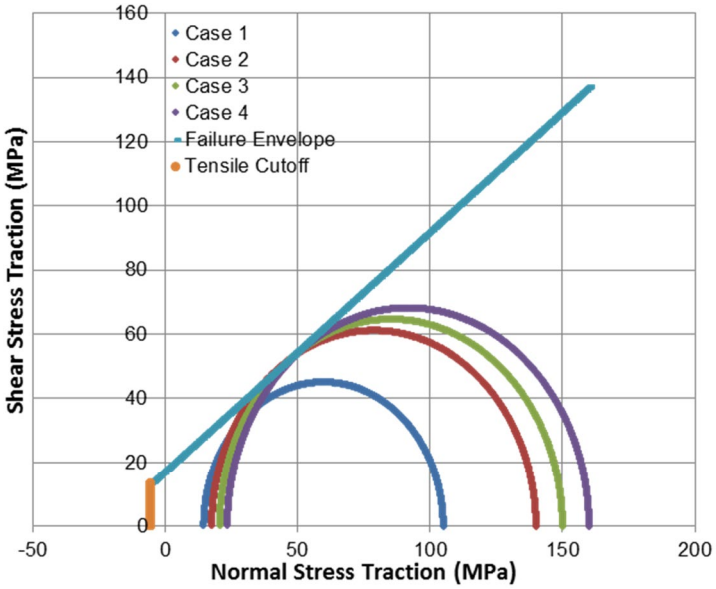

Fig. 8. Mohr circle plot for investigated specimen [21].

V. Conclusions and Future Plans

In conclusion, unconventional reservoirs require new approaches for development, which will take into account physical effects at nano- and micro-scales. The complex of experimental methods and investigations for filling numerical models was developed in this work. Geomechanical, petrophysical dataset and digital imaging data were collected and interpreted.

Future plans include a combination of multiscale digital rock models such as structural, mineral and geomechanical models, building 3D rock model with FEM representation based on an unstructured mesh, numerical simulation of probable fracture propagation scenarios, taking into account uncertainties that appear during study and validation of obtained results on mechanical and DIC experiments.

As a result, it will be possible to predict fracture propagation for tight and unconventional types of hydrocarbon reservoirs. This topic is very interesting for oil and gas companies.

VI. References

[1] S. Chugunov and A. Cheremisin, "Digital Rock Model of Bazhen Formation for Hydrodynamical and Geomechanical Study," in Geomodel 2015-17th science and applied research conference on oil and gas geological exploration and development, 2015.

[2] D. Koroteev et al., "Direct Hydrodynamic Simulation of Multiphase Flow in Porous Rock," Petrophysics, vol. 55, no. 3, pp. 294–303, August 2014 2014.

[3] R. M. Holt, L. Li, and I. Larsen, "Digital Rock Mechanics: A Discrete Way of Approaching Failure," presented at the 51st U.S. Rock Mechanics/Geomechanics Symposium, San Francisco, California, USA, 2017/8/28/, 2017.

[4] Y. Zheng, X. Yin, and Z. Zong, "Estimation of reservoir properties with inverse digital rock-physics modeling approach," presented at the 2017 SEG International Exposition and Annual Meeting, Houston, Texas, 2017/10/23/, 2017.

[5] S. Aliyeva, A. Alabbad, J. P. Daza, and T. Mukerji, "Elasticity, Electrical Conductivity and Permeability in Digital Rocks: A Comparative Study Using Simpleware, NIST, Comsol Multiphysics and Lattice-Boltzmann Algorithms," presented at the 51st U.S. Rock Mechanics/Geomechanics Symposium, San Francisco, California, USA, 2017/8/28/, 2017.

[6] N. Saxena, E. H. Saenger, R. Hofmann, and A. Wiegmann, "Influence of stress and strain loading conditions on elastic and sonic properties of digital rocks," presented at the 2017 SEG International Exposition and Annual Meeting, Houston, Texas, 2017/10/23/, 2017.

[7] M. S. Jouini and S. Vega, "Simulation of Carbonate Rocks Elastic Properties Using 3D X-Ray Computed Tomography Images Based On Discrete Element Method And Finite Element Method," presented at the 46th U.S. Rock Mechanics/Geomechanics Symposium, Chicago, Illinois, 2012/1/1/, 2012.

[8] H. Sun, S. Vega, G. Tao, H. Yong, and B. Li, "Estimation of Petrophysical Parameters of Heterogeneous Carbonate Rock Sample with Multi-Scale CT Images," presented at the Abu Dhabi International Petroleum Exhibition & Conference, Abu Dhabi, UAE, 2016/11/7/, 2016.

[9] H. Sun et al., "Carbonate Rocks: A Case Study of Rock Properties Evaluation Using Multi-Scale Digital Images," presented at the Abu Dhabi International Petroleum Exhibition & Conference, Abu Dhabi, UAE, 2017/11/13/, 2017.

[10] N. Tisato and K. Spikes, "Computation of effective elastic properties from digital images without segmentation," presented at the 2016 SEG International Exposition and Annual Meeting, Dallas, Texas, 2016/1/1/, 2016.
[11] V. Nachev, A. Kazak, and S. Chugunov, "Propagation of Measurement Errors to Uncertainties of Geomechanical Parameters," to be published.
[12] S. Chugunov and A. Kazak, "Building Digital Rock Models for Bazhen Formation with Respect to Uncertainties in Rock Pore-Space," in Geomodel 2016-18th Science and Applied Research Conference on Oil and Gas Geological Exploration and Development, 2016.
[13] V. Shabro, S. Kelly, C. Torres-Verdín, and K. Sepehrnoori, "Pore-Scale Modeling of Electrical Resistivity and Permeability in FIB-SEM Images of Hydrocarbon-Bearing Shale," presented at the SPWLA 54th Annual Logging Symposium, New Orleans, Louisiana, 2013/1/1/, 2013.
[14] D. Katz et al., "Mineralogy Derived Brittleness from the Qemscan: Niobrara Case Study," presented at the SPE Low Perm Symposium, Denver, Colorado, USA, 2016/5/5/, 2016.
[15] A. Kazak et al., "Integration of Large-Area SEM Imaging and Automated Mineralogy-Petrography Data for Justified Decision on Nano-Scale Pore-Space Characterization Sites, as a Part of Multiscale Digital Rock Modeling Workflow," 2017/7/24/.
[16] C. Li, M. Ostadhassan, and L. Kong, "Nanochemo-mechanical characterization of organic shale through AFM and EDS," presented at the 2017 SEG International Exposition and Annual Meeting, Houston, Texas, 2017/10/23/, 2017.
[17] ASTM D2936-08. Standard Test Method for Direct Tensile Strength of Intact Rock Core Specimens, 2008.
[18] ASTM D3967-05. Standard Test Method for Splitting Tensile Strength of Intact Rock Core Specimens, 2005.
[19] GOST, "GOST 28985-91. Rocks. Method of Determination of Deformation Characteristics under Uniaxial Compression," ed. Moscow: Publishing House of Standarts IPK, 1991.
[20] L. Zinsmeister, J. Dautriat, A. Dimanov, J. Raphanel, and M. Bornert, "Mechanical Evolution of an Altered Limestone Using 2D and 3D Digital Image Correlation (DIC)," presented at the 47th U.S. Rock Mechanics/Geomechanics Symposium, San Francisco, California, 2013/1/1/, 2013.
[21] V. Nachev, S. Chugunov, A. Kazak, and A. Myasnikov, "Development of an integrated model of rock fracturing at nano/microscale," in Skoltech & MIT Conference "Shaping the Future: Big Data, Biomedicine and Frontier Technologies", Skolkovo Innovation Center, Moscow, 2017.
[22] S. S. Chugunov, A. V. Kazak, and A. N. Cheremisin, "Integration of X-Ray Micro-Computed Tomography and Focused-Ion-Beam Scanning Electron Microscopy Data for Pore-Scale Characterization of Bazhenov Formation, Western Siberia," Neftyanoe Khozyaystvo - Oil Industry, no. 10, pp. 44–49, 2015.

Optimal Siting, Sizing and Technology Selection of Energy Storage Systems

Timur Sayfutdinov

Abstract - Technology selection, sizing, and siting are the main aspects of the design procedure for Energy Storage Systems (ESSs) for application in power systems. In this paper, we extended instantaneous DC Optimal Power Flow (OPF) problem to formulate a stochastic optimization problem. The optimization problem is designed to find a trade-off between total generation cost of conventional generation units within a transmission network and investment cost for installing ESS. ESS ensures total demand delivery to the end customer and performs spatiotemporal energy arbitrage reducing total generation cost of generation units. A set of representative demand scenarios with the corresponding frequency of occurrence is used within the optimization problem to account for variability of demand profiles. The formulated stochastic optimization problem is convex which guarantees scalability of network size and a number of considered ES technologies, as well as computational tractability. The proposed methodology has been tested on IEEE three generators, nine-bus system for a combination of five ES technologies: lithium-ion; lead-acid; zinc-bromine; vanadium redox flow; sodium sulfur.

Index Terms - energy storage, power system, stochastic optimization, technology selection

I. Nomenclature

Sets and Indices

D	Set of representative demand scenarios, indexed by *d*
J	Set of Energy Storage (ES) technologies, indexed by *n*
K	Set of transmission grid nodes, indexed by *k*
BR	Set of branches within the network, indexed by *km*, where *km* denotes a branch from node *k* to node *m*
I	Set of generation units, indexed by *i*
T	Set of time intervals, indexed by *t*

Given parameters

$C_i^{Gen}(t)$	Generation cost function of the *i*-th generation unit
A_i	The linear part of generation cost function
B_i	Quadratic part of generation cost function
C_j^P, C_j^E	Investment costs of ES technology *j* for every MW and MWh of installed capacity
T_j^{Cal}	Calendar lifetime of ES technology *j*
$\underline{P}_i^{Gen}, \overline{P}_i^{Gen}$	Minimum and maximum power output of the *i*-th generation unit
$P_{d,k}^{Dem}(t)$	Representative demand scenario *d* for node *k*

T. Sayfutdinov is with the Center for Energy Systems, Skolkovo Institute of Science and Technology, Skolkovo Innovation Center, Building 3, Moscow 143026, Russia (e-mail: timur.sayfutdinov@skolkovotech.ru).

$P_{d,k}^{Gen}(t)$	The power output of generation unit at node *k*
$P_{d,k}^{Inj}(t)$	Total net real power injection at node *k*
B_{km}	Susceptance of branch *km*
$\bar{F}_{km}$	Generation limit for real power flow on branch *km*
η_j	Charge/discharge efficiency of ES technology *j*
Δt	Time step
$\underline{k}_j^{E/P}, \overline{k}_j^{E/P}$	Minimum and maximum of energy to power ratio of ES technology *j*
$\overline{SoC}_j, \underline{SoC}_j$	Maximum and minimum state of charge of ES technology *j*

Estimated parameters

$F(d)$	The frequency of occurrence of *d*-th demand scenario

Optimization problem variables

$P_{d,i}^{Gen}(t)$	The scheduled power output of the *i*-th generation unit
$\delta_{d,k}(t)$	Voltage angle at node *k*
$P_{d,j,k}^{ES+}(t)$	The positive part of the scheduled power output of ES technology *j* at node *k*
$P_{d,j,k}^{ES-}(t)$	The negative part of the scheduled power output of ES technology *j* at node *k*
$E_{d,j,k}^{ES}(t)$	The charge of ES technology *j* at node *k*
$\overline{P}_{j,k}^{ES}$	Rated power capacity of ES technology *j* at node *k*
$\overline{E}_{j,k}^{ES}$	The rated energy capacity of ES technology *j* at node *k*

II. Introduction

Energy Storage Systems (ESSs) are currently being employed within distribution and transmission networks to provide a variety of network services such as control of voltage and frequency, power output smoothing of renewable energy sources, and peak shaving. The inclusion of ESS into the grid allows an increased utilization factor for the existing assets, and can often ensure reliable network operation with a lesser degree of network redundancy. However, the selection of Energy Storage (ES) technology, size, and site is critical for the increase of ESS profitability in different applications.

The literature on ESS can be divided into three major categories: ESS scheduling and operation [1]-[7]; ESS sizing and/or siting [8]-[19]; ES technology selection [20]-[22]. To obtain the most value from ESS functioning, the design procedure (siting, sizing, and technology selection) has to be done with respect to effective scheduling and operation of ESS. Thus, considering optimal scheduling and operation of ESS along with optimal siting, sizing, and technology selection is vital for determining the most cost-effective combination of ESS design parameters.

A. ESS Scheduling and Operation

In [1]-[4] scheduling and operation of ESS is performed to maximize the profit that an owner of ESS can gain from the energy market. In [5], [6] ESS is used in conjunction with Renewable Energy Sources (RESs) to provide additional services such as smoothing power fluctuations of RES or keeping a spinning reserve. In Sachs ***et al.*** [7] ESS are used for power balancing in an islanded microgrid. Even though the considered papers on operation and scheduling of ESS have different objectives, they have similarities. Optimal scheduling and operation are done for a given ESS of predefined technology, size, and site. One of the main attributes of the proposed

methods is short computational time, as they all have to assure real-time response.

B. ESS Siting and Sizing

Usually, siting and sizing are done with respect to optimal scheduling of assets within a network. A number of methodologies for optimal siting and sizing exists in the literature: exhaustive whole enumeration approach [8], [9]; statistical analysis of power and energy scarcities [10]; heuristic algorithms [11]-[13]; convex optimization [14]; mixed-integer linear programming [15]-[18]; neural networks [19]. To account for the diversity of network scenarios and ensure computational tractability, the authors of [16]-[18] apply different clustering techniques to generate a set of representative scenarios based of historical data of demand. Siting and sizing of ESS relate to the design problem and does not require fast computation, as a real-time response is not expected. For that reason, the authors of siting and sizing papers consider more detailed and more computationally demanding models of ESS.

C. ESS Technology Selection

Most of the considered optimal operation, siting, and sizing papers are limited to a single ES technology, usually, Lithium-ion (Li-ion) or Vanadium Redox Flow Battery (VRFB) without any numerical justification for the selection of a particular technology. However, Munoz-Vaca ***et al.*** [23] have proven that Hybrid ESS (HESS) might be more beneficial than a single ES technology. There are a number of ES technologies that are successfully utilized in power systems, such as Zinc-Bromine flow batteries (ZnBr), Sodium Sulphur batteries (NaS), lead-acid batteries, Supercapacitors (SCs), all of which are economically and technically competitive with the popular Li-ion and VRFB.

The best practice of ESS application shows that each ES technology has its niche. Redox flow batteries are well suited for large-scale energy storage applications due to high power and energy capability, scalability and high cycle lifetime [8]. Lead-acid batteries offer a mature and well-researched technology at a low cost [24] but suffer from a low cycle lifetime. Relatively expensive Li-ion batteries compete with lead-acid technology in the areas where high power capability is required, but Li-ion technology guarantees longer lifetime and higher round-trip efficiency. NaS batteries are widely used in Germany, France, USA, UAE, and Japan for power quality and time shifting applications [25]. Electrochemical double-layer capacitors or SC are used for very fast and reliable applications such as power quality control and power smoothing of RESs [9] where one million charge-discharge cycles can be achieved in less than ten years, but the cost of energy capacity is too high for energy demanding applications. However, a field of applications for combinations of ES technologies has not been studied yet.

Technology selection for ESS has not been thoroughly investigated as operation and sizing. Pham and Mansson in [20] suggested a fuzzy logic approach to perform multi-criteria analysis of different ES technologies for various applications. But the main drawback of the approach is that the definition of the fuzzy logic rules is subjective and relies only on the experience of the designer. Miranda ***et al.*** [21] apply a whole enumeration and consequent simulation method for sizing and technology selection. All of the proposed methodologies are found to be inefficient.

D. Optimal Power Flow

Standard DC Optimal Power Flow (OPF) problem is a tool to optimally schedule all assets within a network and get minimum operational cost of a whole system [26]. Standard DC OPF problem is instantaneous, it is solved individually for every separate instance of time, as by default the problem does not contain any means to store and shift energy in time. It means that generation has to be equal to consumption at every instance of time. To include ES in the problem, a standard DC OPF has to be extended to a time-dependent problem, where the produced energy can be stored and shifted in time by means of ESS. It means that an optimization problem has to be formulated and solved for every time instance with respect to each other simultaneously.

E. Contributions of the Paper

The methodology presented in the paper is aimed to solve the optimal siting, sizing, and technology selection of ESS. The criterion for the optimality in this research is the minimum total operational cost of a power system. To ensure the most cost-effective combination of site, size, and technology of ESS, the design procedure is done with respect to optimal scheduling of all assets within a network, including conventional generation units and ES units. The proposed approach extends a standard DC OPF problem by incorporation of ESS models into it.

The methodology allows considering several ES technologies including their combinations to provide the optimal solution. The method is technology agnostic, which means that any ES technology can be considered within the optimization problem. Stochastic optimization problem ensures optimal results that take into account all representative scenarios of demand with a corresponding frequency of occurrence simultaneously. The method has been tested on a particular case-study network considering actual historical data of demand.

III. Case study

This section presents a particular case-study transmission network, ES characteristics of considered technologies, and historical demand data used in the analysis.

A. Transmission Network

IEEE three generators, nine-bus transmission network has been used as the case-study network. The considered case-study network with corresponding power lines limits is shown in Fig. 1. It is assumed that ESS, comprising any ES technology combinations, can be potentially installed at every bus if it provides the minimum operational cost of the system.

The considered transmission network contains three conventional generation units at the nodes one, two and three. The power output of generation units is limited by adjacent power line limits. Power consumers are located at the nodes five, seven and nine.

B. Generation Units

It is natural that a power system contains a number of generation assets with different production characteristics, such as generation cost function and power output limits. Usually, generation cost function is characterized by a quadratic function (1)

$$C_i^{Gen}(t) = A_i P_i^{Gen}(t) + B_i P_i^{Gen^2}(t). \qquad (1)$$

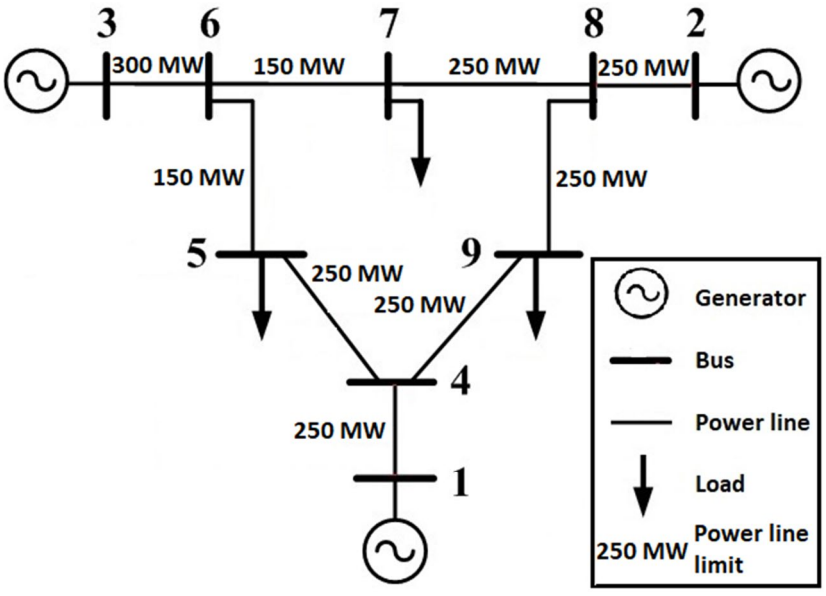

Fig. 1. Case study transmission network.

The considered transmission network contains three generation units, indexed by the adjacent bus numbers. Table I provides values of a linear and quadratic part of generation cost function (1) for each generation unit.

Table I. Generation cost parameters

i	A_i	B_i
1	5	0.11
2	1.2	0.085
3	1	0.1225

C. Energy Storage Characteristics

The proposed methodology has been formulated to select the most cost-effective combination of site, size, and technology to minimize the overall operational cost of the whole system. The methodology is not ES type specific and any technology, for which data are available, could be included. The ES technologies and their characteristics used within the analysis are presented in Table II. The optimization problem is formulated with respect to round-trip efficiency, calendar lifetime, investment costs and energy to power ratio. Round-trip efficiency is the main characteristic of ESS that shows ratio of input energy to output energy. Calendar lifetime defines aging degradation period of a particular ES technology, even if ESS is idle. Investment costs for power and energy capacities define costs for every MW and MWh of installed capacity. Limited range of energy to power ratio (charge/discharge rate) defines scalability constraints of a particular ES technology.

Table II. ES Technology parameters

N	Technology	Round-trip efficiency, (%)	Calendar Lifetime, (years)	Energy Capacity Cost, ($/kWh)	Power Capacity Cost, ($/kW)	Energy to Power ratio
1	Li-ion	95	15	490	325	0.1 - 6
2	ZnBr	70	15	320	320	2 - 8
3	VRFB	70	20	490	325	4 - 15
4	NaS	75	15	285	285	6 - 7.2
5	Lead-acid	85	10	260	320	0.25 - 6

D. Demand Data

Demand scenarios are considered as input data for an optimization problem. To account for variability and seasonal deviation of demand profiles, at least one year of historical data is required for the analysis. Power consumption data were taken from Customer-Led Network Revolution project [27]. A total of 365 days of historical demand data with a resolution of 10 minutes was used for this study. The data were averaged to one-hour intervals to comply with the time step used in the optimization problem. The recursive clustering technique was applied to the historical data of 365 demand profiles to derive five representative scenarios and the corresponding frequency of occurrence [28].

IV. METHODOLOGY

This section contains the mathematical formulation of the stochastic optimization problem for siting, sizing and technology selection of ESS. The optimization problem extends instantaneous DC OPF problem [26] to the time-dependent problem of optimal scheduling of assets, siting, sizing, and technology selection of ESS.

The objective function is designed to find a trade-off between generation cost of generation units and per diem cost for ESSs to be installed

$$min \sum_{d=1}^{D} F(d) \sum_{t=1}^{T} \sum_{i=1}^{I} \left[-A_i P_i^{Gen}(t) + B_i P_i^{Gen^2}(t) \right] + \\ + \sum_{k=1}^{K} \sum_{j=1}^{J} \frac{\overline{P}_{j,k}^{ES} \cdot C_j^P + \overline{E}_{j,k}^{ES} \cdot C_j^E}{T_j^{Cal}} \quad (2)$$

with respect to:

$$P_{d,i}^{Gen}(t);\ \delta_{d,k}(t);\ P_{d,j,k}^{ES+}(t); P_{d,j,k}^{ES-}(t);\ E_{d,j,k}^{ES}(t);\ \overline{P}_{j,k}^{ES};\ \overline{E}_{j,k}^{ES}.$$

To retain convexity of the optimization problem, the scheduled power output of ESS is divided into two parts – a positive and a negative one:

$$P_{d,j,k}^{ES+}(t) + P_{d,j,k}^{ES-}(t) = P_{d,j,k}^{ES}(t). \quad (3)$$

Here we define the positive value of power as consumption (charging) and a negative value as generation (discharging). Hence, the negative sign in the first term of the objective function (2) implies that generation cost of generation units is positive. The second term of the objective function defines per diem cost of the ESSs to be installed within the network.

The constraints of the optimization problem are presented in (4)-(15). Real power production constraints for each generation unit are satisfied by inequality (4)

$$\underline{P}_i^{Gen} \le P_{d,i}^{Gen}(t) \le \overline{P}_i^{Gen}, \forall\ d \in D, i\ \in I, t\ \in T. \quad (4)$$

Real power balance at each node is satisfied by equality (5)

$$\sum_{j=1}^{J} \left[P_{d,j,k}^{ES+}(t) + P_{d,j,k}^{ES-}(t) \right] + P_{d,k}^{Dem}(t) + P_{d,k}^{Gen}(t) + \\ + P_{d,k}^{Inj}(t) = 0, \forall\ d \in D, k\ \in K, t\ \in T, \quad (5)$$

where power generation by a generation unit at node k is defined in (6)

$$P_{d,k}^{Gen}(t) = \begin{cases} P_{d,i}^{Gen}(t) & , i = k \\ 0 & \text{otherwise} \end{cases} \quad (6)$$

Real power flow of every branch is limited by its thermal constraints (7)

$$\left| B_{km} \cdot \left(\delta_{d,k}(t) - \delta_{d,m}(t) \right) \right| \le \bar{F}_{km}, \quad (7)$$

$$\forall\ d \in D, t\ \in T, km\ \in BR.$$

Total net real power injection at node k is defined by equality

$$P_{d,k}^{Inj}(t) = \sum_{km}^{BR} \left| B_{km} \cdot \left(\delta_{d,k}(t) - \delta_{d,m}(t) \right) \right|, \quad (8)$$

$$\forall\ d \in D, k\ \in K, t\ \in T.$$

Voltage angle at reference node 1 for every instance of time is set to 0 in (9)

$$\delta_{d,1}(t) = 0, \forall\, d \in D, t\ \in T. \tag{9}$$

Charge and discharge power of ESS are limited by inequalities (10) and (11)

$$0 \le P_{d,j,k}^{ES+}(t) \le \overline{P}_{j,k}^{ES}, \forall\, d \in D, j\ \in J, k\ \in K, t\ \in T, \tag{10}$$

$$-\overline{P}_{j,k}^{ES} \le P_{d,j,k}^{ES-}(t) \le 0, \forall\, d \in D, j\ \in J, k\ \in K, t \in T. \tag{11}$$

State of charge of ESS is limited by the corresponding energy rating in inequality (12)

$$0 \le E_{d,j,k}^{ES}(t) \le \overline{E}_{j,k}^{ES}, \forall\, d \in D, j\ \in J, k\ \in K, t\ \in T, \tag{12}$$

where the state of charge of the ESS is defined by equality

$$\begin{aligned} E_{d,j,k}^{ES}(t+1) = {} & E_{d,j,k}^{ES}(t) \\ & + \left(P_{d,j,k}^{ES+}(t) + P_{d,j,k}^{ES-}(t)\right)\Delta t - \\ & -(1-\eta_j)\cdot\left(P_{d,j,k}^{ES+}(t) - P_{d,j,k}^{ES-}(t)\right)\Delta t, \\ & \forall\, d \in D, j\ \in J, k\ \in K, t\ \in T. \end{aligned} \tag{13}$$

The net daily energy charge of ESS is set to zero by equality

$$E_{d,j,k}^{ES}(1) = E_{d,j,k}^{ES}(T+1), \forall\, d \in D, j\ \in J, k\ \in K. \tag{14}$$

Energy to power ratio of each ES technology is satisfied by inequality (15)

$$\underline{k}_j^{E/P} \le \frac{\overline{E}_{j,k}^{ES}}{\overline{P}_{j,k}^{ES}} \le \overline{k}_j^{E/P}, \forall\, j\ \in J, k\ \in K. \tag{15}$$

The proposed stochastic optimization problem is convex, meaning that global optimum can be found using an interior-point method or any other applicable method.

V. Results and discussion

The methodology described in the previous section has been applied to the case-study provided in section III. Stochastic optimization problem has been formulated for IEEE three generators, nine-bus system, and five representative demand scenarios with a corresponding frequency of occurrence. The optimization problem contains 17,955 variables and 34,245 constraints. It has been solved using CVX modeling system. Table III presents the optimal solution of the optimization problem, and Fig. 2 represents the optimal site, size, and technology of ESS for the given case-study graphically. The solution of the optimization problem provides Zinc-Bromine ESS of 6.4 MW and 12.8 MWh of installed power and energy capacities at bus seven as the best combination that ensures total load delivery and minimum operational cost of the power system.

Table III. The optimal solution of the optimization problem

Bus #	Tech-nology	Power Capacity, MWh	Energy Capacity, MWh	Investment Cost, $	Savings ,$
7	ZnBr	6.4	12.8	6.1M	7.3M

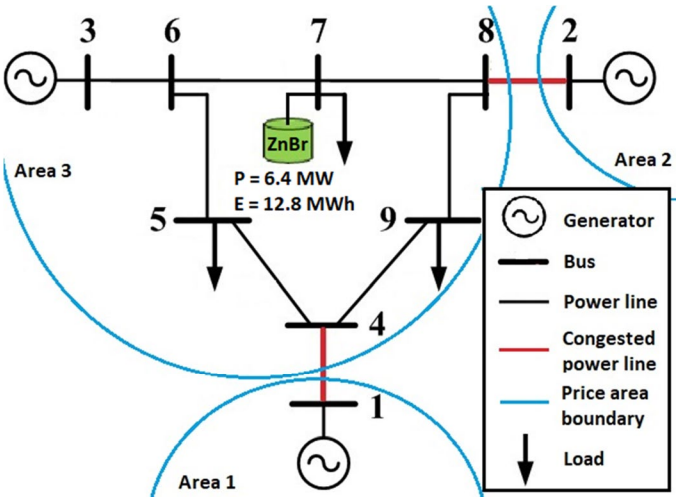

Fig. 2. Optimal solution.

The optimal location, size, and technology of ESS have been found with respect to the optimal scheduling of all assets within transmission network. Fig. 3 provides optimal scheduling of generation units for one of the representative scenarios. It can be noted from Fig. 3 that the cheapest generation unit produces the highest amount of power until it reaches its output limit. Then a moderately expensive generator increases its generation until it reaches its power output limit. The most expensive generation unit ramps up only after all the cheaper units are saturated. Two congested power lines break the transmission network into three price areas (Fig. 2) with different locational marginal prices for energy generation.

Scheduling of ESS is also done in an optimal manner. Fig. 4 provides energy price profile and state of charge value of Zinc-Bromine ESS installed at bus seven during one of the representative scenarios. It can be noted from Fig. 4 that ESS charges during the valley price period and discharges at peak price period, which gives the highest revenue from spatiotemporal energy arbitrage.

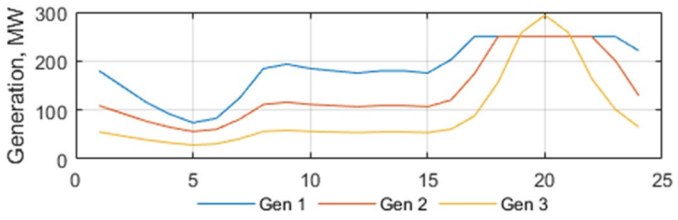

Fig. 3. Optimal scheduling of generation units.

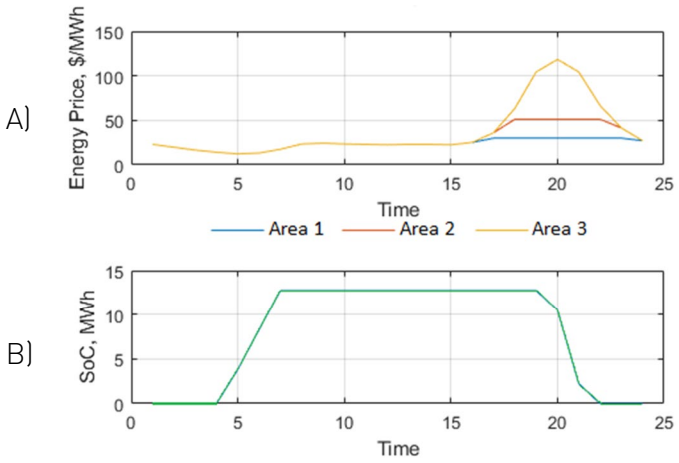

Fig. 4. A) Energy price of the congested network; B) State of charge of Zinc-Bromine ESS at bus 7.

VI. Conclusions

This paper addresses optimal siting, sizing, and technology selection of ESS problem. The proposed methodology extends standard DC OPF problem to time-dependent problem that considers optimal scheduling of all assets within a network. The stochastic optimization problem takes into account a number of representative demand scenarios with a corresponding frequency of occurrence and finds a trade-off between generation cost of conventional generation units and investment cost for ESS. Thus, ESS is installed only if its installation is economically viable and/or required to satisfy all demand.

The proposed methodology has been tested on IEEE three generators, nine-bus network. A historical data of demand has been clustered to 5 representative scenarios of demand with a corresponding frequency of occurrence. Five electrochemical ES technologies have been considered within the optimization problem. The optimal solution of siting, sizing, and technology selection problem has been found with respect to optimal scheduling of all assets within transmission network.

The proposed optimization problem is convex and easily scalable to much bigger networks and a higher number of considered ES technologies.

VII. References

[1] J. Donadee, "Optimal operation of energy storage for arbitrage and ancillary service capacity: The infinite horizon approach," in 45th North American Power Symposium, NAPS 2013, 2013, pp. 1–6.

[2] K. Abdulla et al., "Optimal Operation of Energy Storage Systems Considering Forecasts and Battery Degradation," IEEE Trans. Smart Grid, vol. 9, no. 3, pp. 2086–2096, 2018.

[3] N. Jayasekara, M. A. S. Masoum, and P. J. Wolfs, "Optimal Operation of Distributed Energy Storage Systems to Improve Distribution Network Load and Generation Hosting Capability," IEEE Trans. Sustain. Energy, vol. 7, no. 1, pp. 250–261, 2016.

[4] D. Greenwood, N. Heyward, N. Wade, P. Mehta, P. Taylor, and P. Papadopoulos, "Scheduling power and energy resources in the Smarter Network Storage project," in CIRED 23rd International Conference and Exhibition on Electricity Distribution, 2015, pp. 1–5.

[5] B. Aluisio, M. Dicorato, G. Forte, M. Trovato, and P. Bari, "Hybrid Energy Storage System Optimization for Improving Wind Power Integration," in Power Systems Computation Conference (PSCC), 2016, 2016, pp. 1–6.

[6] R. Halvgaard, L. Vandenberghe, N. K. Poulsen, H. Madsen, and J. B. Jørgensen, "Distributed Model Predictive Control for Smart Energy Systems," IEEE Trans. Smart Grid, vol. 7, no. 3, pp. 1675–1682, 2016.

[7] J. Sachs and O. Sawodny, "A Two-Stage Model Predictive Control Strategy for Economic Diesel-PV-Battery Island Microgrid Operation in Rural Areas," IEEE Trans. Sustain. Energy, vol. 7, no. 3, pp. 903–913, 2016.

[8] T. K. A. Brekken, A. Yokochi, A. Von Jouanne, Z. Z. Yen, H. M. Hapke, and D. A. Halamay, "Optimal Energy Storage Sizing and Control for Wind Power Applications," IEEE Trans. Sustain. Energy, vol. 2, no. 1, pp. 69–77, 2011.

[9] T. Kovaltchouk, B. Multon, H. Ben Ahmed, J. Aubry, and P. Venet, "Enhanced Aging Model for Supercapacitors Taking into Account Power Cycling: Application to the Sizing of an Energy Storage System in a Direct Wave Energy Converter," IEEE Trans. Ind. Appl., vol. 51, no. 3, pp. 2405–2414, 2015.

[10] M. R. Aghamohammadi and H. Abdolahinia, "A new approach for optimal sizing of battery energy storage system for primary frequency control of islanded Microgrid," Int. J. Electr. Power Energy Syst., vol. 54, pp. 325–333, 2014.

[11] X. Xie, H. Wang, S. Tian, and Y. Liu, "Optimal capacity configuration of hybrid energy storage for an isolated microgrid based on QPSO algorithm," in Proceedings of the 5th IEEE International Conference on Electric Utility Deregulation, Restructuring and Power Technologies, DRPT 2015, 2015, pp. 2094–2099.

[12] Y. Luo, L. Shi, and G. Tu, "Optimal sizing and control strategy of isolated grid with wind power and energy storage system," Energy Convers. Manag., vol. 80, pp. 407–415, 2014.
[13] J. Xiao, L. Bai, Z. Zhang, and H. Liang, "Determination of the optimal installation site and capacity of battery energy storage system in distribution network integrated with distributed generation," IET Gener. Transm. Distrib., vol. 10, no. 3, pp. 601–607, 2016.
[14] K. Baker, G. Hug, and X. Li, "Energy Storage Sizing Taking into Account Forecast Uncertainties and Receding Horizon Operation," IEEE Trans. Sustain. Energy, vol. 8, no. 1, pp. 331–340, 2017.
[15] H. Pandzic, Y. Wang, T. Qiu, Y. Dvorkin, and D. S. Kirschen, "Near-Optimal Method for Siting and Sizing of Distributed Storage in a Transmission Network," IEEE Trans. Power Syst., vol. 30, no. 5, pp. 2288–2300, 2015.
[16] Y. Dvorkin, R. Fernandez-Blanco, D. S. Kirschen, H. Pandzic, J. P. Watson, and C. A. Silva-Monroy, "Ensuring Profitability of Energy Storage," IEEE Trans. Power Syst., vol. 32, no. 1, pp. 611–623, 2017.
[17] T. Qiu, B. Xu, Y. Wang, Y. Dvorkin, and D. S. Kirschen, "Stochastic Multistage Coplanning of Transmission Expansion and Energy Storage," IEEE Trans. Power Syst., vol. 32, no. 1, pp. 643–651, 2017.
[18] R. Fernandez-Blanco, Y. Dvorkin, B. Xu, Y. Wang, and D. S. Kirschen, "Optimal Energy Storage Siting and Sizing: A WECC Case Study," IEEE Trans. Sustain. Energy, vol. 8, no. 2, pp. 733–743, 2017.
[19] G. Giannakoudis, A. I. Papadopoulos, P. Seferlis, and S. Voutetakis, "Optimum design and operation under uncertainty of power systems using renewable energy sources and hydrogen storage," Int. J. Hydrogen Energy, vol. 35, no. 3, pp. 872–891, 2010.
[20] C. Pham and D. Månsson, "Suitability analysis of Fuzzy Logic as an evaluation method for the selection of energy storage technologies in Smart Grid applications," in Smart Electric Distribution Systems and Technologies (EDST), 2015 International Symposium on, 2015, pp. 452–457.
[21] I. Miranda, N. Silva, and H. Leite, "A Holistic Approach to the Integration of Battery Energy Storage Systems in Island Electric Grids with High Wind Penetration," IEEE Trans. Sustain. Energy, vol. 7, no. 2, pp. 775–785, 2016.
[22] M. Martinez, M. G. Molina, and P. E. Mercado, "Optimal Storage Technology Selection and Sizing for Providing Reserve to Power Systems with High Penetration of Wind Generation," IEEE Lat. Am. Trans., vol. 13, no. 9, pp. 2983–2990, 2015.
[23] S. Munoz Vaca, C. Patsios, and P. Taylor, "Enhancing Frequency Response of Wind Farms using Hybrid Energy Storage Systems," in Renewable Energy Research and Applications (ICRERA), 2016 IEEE International Conference on, 2016, pp. 325–329.
[24] International Electrotechnical Commission, "IEC White Paper: Electrical Energy Storage Electrical Energy Storage," Geneva, Switzerland, 2011.
[25] B. S. Morozumi, "Japanese Experience in Energy Storage for a Distribution Network with High-Penetration Renewable Energy," IEEE Electrif. Mag., vol. 3, no. 3, pp. 4–12, 2015.
[26] J. Sun and L. Tesfatsion, "DC Optimal Power Flow Formulation and Solution Using QuadProgJ ∗," no. 6014, pp. 1–62, 2010.
[27] Customer-Led Network Revolution, "Domestic smart meter customers on time of use tariffs," 2016. [Online]. Available: http://www.networkrevolution.co.uk/resources/project-data/.
[28] B. Pitt, "Applications of Data Mining Techniques to Electric Load Profiling," University of Manchester, 2000.

Thermodynamics of Methane Hydrate

D.V. Sergeeva*, V.A. Istomin

Abstract - The thermodynamic analysis of available experimental data on three-phase equilibria "methane – ice – methane hydrate" and "methane – liquid water – methane hydrate" is presented. It is found that there is practically no experimental data in the temperature range 260-270 K as well as large errors in the data near 273 K. A new thermodynamic method is proposed that makes it possible to reveal the thermodynamic inconsistency of the experimental data and thereby ensure their correct smoothing and interpolation. Smoothed data on three-phase equilibria of methane hydrate was obtained, which made it possible to calculate correctly the enthalpies of methane hydrate decomposition to ice and water and to estimate the hydrate number n at the quadrupole point.

Index Terms - phase equilibrium, gas hydrate, hydrate numbers, methane

I. Nomenclature

i	ice phase
h	hydrate phase
w	water phase
n	number of water molecules per one guest molecule
v_i	the ratio of the number of type i cavities (i = 1, 2) to the number of water molecules in the hydrate unit cell
θ_i	degree of filling of the small and large cavities
x	mole fraction of gas in hydrated form
M	the guest molecule
ΔH_w	the enthalpy of decomposition of one mole of hydrate per one mole of gas and *n* moles of water at the quadrupole point (J/mol)
ΔH_i	the enthalpy of decomposition of one mole of hydrate per one mole of gas and *n* moles of ice at the quadrupole point (J/mol)
ΔV_w	the change of the molar volume of the system during the decomposition of the hydrate into water and gas (cm^3/mol)
ΔV_i	the change of the molar volume of the system during the decomposition of the hydrate into water and gas (cm^3/mol)
P	gas pressure (MPa)
f	gas fugacity (MPa)
T	temperature (K)
T_q	temperature in the quadrupole point (K)
ρ_q	density of gas in the quadrupole point (g/cm^3)

D. V. Sergeeva is with the Center of Hydrocarbon Recovery, Skolkovo Institute of Science and Technology, Skolkovo Innovation Center, Building 3, Moscow 143026, Russia (e-mail: daria.sergeeva@skolkovotech.ru).
V. A. Istomin is with the Center of Hydrocarbon Recovery, Skolkovo Institute of Science and Technology, Skolkovo Innovation Center, Building 3, Moscow 143026, Russia (e-mail: v.istomin@skoltech.ru).

$\boldsymbol{\lambda}$ a molar enthalpy difference between water and ice (J/mol)

$\Delta\boldsymbol{\mu_w}$ the difference between chemical potentials of water in an empty hydrate lattice and the liquid phase (J/mol)

$\boldsymbol{\mu_j}$ the chemical potential of *jth* component of hydrate formed in equilibrium with hydrate (J/mol)

II. Introduction

Permafrost occupies about 25% of the world's land and 67% of the land of Russia, including Arctic shelf. Oil and gas reserves and resources in Russia are mainly situated in the permafrost area. The development of oil and gas fields in the Arctic is complicated by many factors. One of the factors is gas hydrates which were discovered more than 200 years ago. Gas hydrates are crystalline substances like ice or snow, which are formed from gases and water phases (liquid water, ice or water vapor).

Some new Russian gas and gas-condensate fields with very low formation temperatures (282-290 K) are now ready for development. The thermodynamic conditions of such fields are very close to hydrate formation conditions. During field development, the technogenic hydrates may occur in the bottom-hole zones, lift pipes, in-field pipelines and field gas processing systems.

Phase equilibrium data of gas hydrates and the knowledge of hydrate forming conditions are essential for testing existing thermodynamic models or designing new thermodynamic models for phase behavior of hydrocarbon systems.

III. Methods

A. Information about gas hydrates

Gas hydrates are solid crystalline substances. They may be formed at appropriate thermobaric conditions from liquid water (or water solution), ice, water vapor and some low-molecular gases.

The general formula of a gas hydrate is

$$\boldsymbol{M \cdot nH_2O}, \qquad (1)$$

where M means the guest molecule, n is the number of water molecules per one guest molecule. Number n is a variable and depends on the type of gas, pressure and temperature.

In the structure of gas hydrates, water molecules form a framework (host lattice) in which cavities are present [1]. It is established that the carcass cavities are usually 12- ("small" cavities), 14-, 16- and 20-hedron ("large" cavities), slightly deformed with respect to the ideal shape. These cavities can be occupied by gas molecules ("guest molecules"). The gas molecules are connected with the water skeleton by van der Waals bonds. Cavities, combining among themselves, form continuous structures of various types. According to the accepted classification, they are called CS, TS, HS – respectively cubic, tetragonal and hexagonal structure. Hydrates of the types CS-I, CS-II are most often encountered, while the others are metastable. Each structure has two types of cavities, small and large. The unit cell of CS-I consists of 46 water molecules and they form 2 small cages (D) and 6 large ones (T). The unit cell of CS-II consists of 136 water molecules and they form 16 small cages (D) and 8 large ones (T).

Crystallochemical constants $\boldsymbol{v_i}$ are introduced for the convenience of describing the ratio of the number of cavities and water molecules in a unit cell. For the structure I we have $v_1 = \frac{1}{23}$; $v_2 = \frac{3}{23}$; and for structures II we obtain $v_2 = \frac{2}{17}$; $v_2 = \frac{1}{17}$. So, for example, $v_2 = \frac{1}{23}$ characterizes the ratio of the number of small cavities to the number of water molecules in the unit cell of the hydrate structure I [2].

The composition of the individual hydrate can be given in at least three ways: by the number n, assuming the hydrate formula (1); mole fraction x of gas in the clathrate phase, assuming the hydrate formula $(1-x)H_2O \cdot x \cdot M$ and the degrees of filling θ_1, θ_2 of small and large cavities, respectively. The degree of filling, by definition, can vary from zero to one. Methods for specifying the composition are interrelated by means of simple algebraic relations

$$\boldsymbol{n = \frac{1-x}{x};\ n^{I} = \frac{23}{\theta_1^{I} + 3\theta_2^{I}};\ n^{II} = \frac{17}{2\theta_1^{II} + \theta_2^{II}}.} \qquad (2)$$

The upper indices I and II refer to the type of hydrate structure. The formulas of the hydrates with structural stoichiometry corresponding to the full occupancy of the cavities by guest gas molecules are presented below in Table I.Gas hydrates are compounds of variable composition and the values n, θ_1, θ_2 depend on temperature, pressure and other conditions for obtaining hydrates.

Table I. The limiting hydrate formulas

Character of filling	Hydrate structure	
	I	II
Filling only large cavities	$M \cdot 7.67H_2O$	$M \cdot 17H_2O$
Filling both cavities	$M \cdot 5.75H_2O$	$M \cdot 5.67H_2O$
Filling small cavities with one gas, and large cavities with another gas	$M_I \cdot 3M_{II} \cdot 23H_2O$	$2M_I \cdot M_{II} \cdot 17H_2O$

Hydrate three-phase equilibria for different gases are presented in Fig. 1 [3]. Here we have a three-phase gas-ice-hydrate equilibrium at a temperature below 273 K and a three-phase gas-water-hydrate equilibrium at a temperature above 273 K.

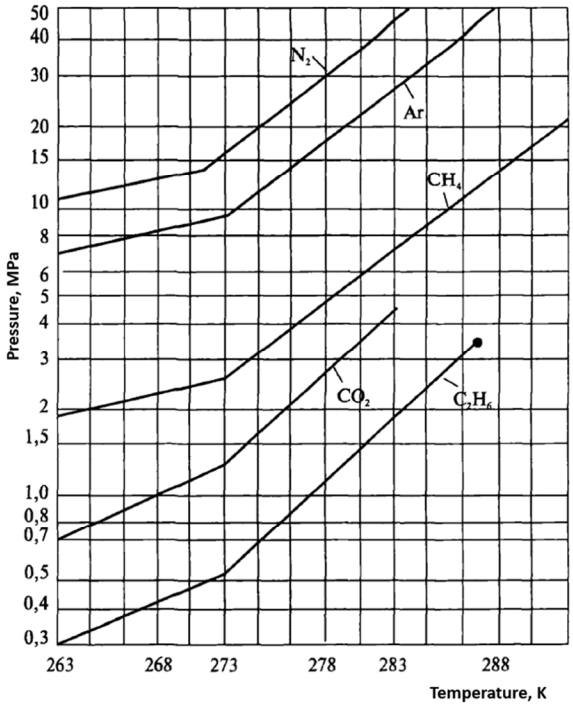

Fig. 1. Gas-ice-hydrate equilibrium, gas-water-hydrate equilibrium [3].

The formula for calculating the hydrate number is

$$n = \frac{\Delta H_w - \Delta H_i}{\lambda} = \frac{T_q\left(\left(\frac{dP}{dT}\right)\Big|_{(w)} \cdot \Delta V_w - \left(\frac{dP}{dT}\right)\Big|_{(i)} \cdot \Delta V_i\right)}{\lambda} \quad (3)$$

or

$$n = \frac{T_q}{\rho_{q^\lambda}}\left(\left(\frac{dP}{dT}\right)\Big|_{(w)} \cdot \Delta V_w - \left(\frac{dP}{dT}\right)\Big|_{(i)} \cdot \Delta V_i\right), \quad (4)$$

where n – hydrate number, T_q – temperature in the quadrupole point, ρ_q – density of gas in the quadrupole point, λ – a molar enthalpy difference between water and ice at 273.15 K.

The calculation of the hydrate number is sensitive to the slope of the curves near 273.15 K. Good agreement is observed between some literature sources for pure methane [4]-[7], but in some sources [8]-[10] data do not correspond to values of the degrees of filling the cavities [2].

The conventional model of the hydrated phase is the ideal clathrate model, developed in the mid-1950s in the works of Barrera and van der Waals. The hydrate formation process in this model is considered as the sorption of gas molecules in the cavity of the hydrates carcass, and in itself (i.e., the unfilled) the lattice is thermodynamically unstable (metastable). Gas molecules stabilize the hydrate carcass. The sorption process is described by the Langmuir isotherm (i.e., the interaction of the included molecules is not taken into account), introducing Langmuir constants C_1 and C_2, respectively, for small and large cavities. Within this model, cavities are never fully filled. Next, the hydrate is considered as a solid solution. The concept of the chemical potential of water μ_w is introduced, with μ_w^0 – the chemical potential of the hypothetical empty hydrate lattice.

$$\mu_h = \mu_h^0(T, P_0) - v_1 RT\, ln(1 + C_1 f) - v_2 RT\, ln(1 + C_2 f)$$

$$\mu_w = \mu_w^0 + V_w \cdot (P - P_0) + RT\, ln(1 - x) \quad (5)$$

$$\mu_i = \mu_i^0(T, P_0) + V_i \cdot (P - P_0),$$

where μ_h, μ_w, μ_i are the chemical potential of the hypothetical of hydrate, water, ice, f – fugacity, V_w, V_i are the molar volumes of water, ice.

B. Analysis of experimental data at the phase equilibrium of methane-water (ice) -hydrate

Three-phase equilibria of gas-water-hydrate and gas-ice-hydrate are of practical interest. Methane is the main composition component of the natural gas. Therefore, in the first place, it is necessary to analyze the experimental data on methane hydrates.

A large number of experimental investigations have been devoted to the study of methane hydrate formation in free volume. Experiments on phase equilibria are made in dynamic or static conditions. The main element of the static type installations is the cell (hydrate chamber or reactor-crystallizer) in which hydrate is formed (or decomposed). There is an exactly adjustable gas delivery system and its saturation with water vapor, as well as temperature and pressure monitoring equipment. The cell allows a visual approach (viewing window). To

accelerate the achievement of equilibrium, the following methods of mixing the contents of the cell are used: shaking the chamber, magnetic stirrer, ultrasound emitter; applying an external magnetic field, adding to the liquid phase of the crystallization nuclei.

Experiments on the study of hydrate equilibrium on pure methane began in 1940 [8] on special hydrate equipment. Five equilibrium points were obtained in the temperature range 262.4÷270.9 K at a pressure range of 1.793÷2.392 MPa. Further study of the hydrate equilibrium on pure methane at temperatures negative in Celsius was done in [9], [11]-[14], and at positive temperatures in the works [8], [9], [15]-[24] as summarized in Table II and Table III.

Table II. Literature Data on Methane-Ice-Hydrate Equilibrium

Author(s)	Range of T/K	Range of P/MPa	Number of points, N
Chueh (1973)	241.5÷273.15	0.896÷2.62	4
Deaton and Frost (1946)	262.4÷270.9	1.793÷2.392	5
Falabella (1975)	148.8÷191.3	0.005÷0.09	5
Makogon et al. (1994)	190.15÷262.4	0.082÷1.798	6
Hachikubo et al. (2002)	268.4÷271.3	2.324÷2.527	2

Table III. Literature Data on Methane-Water-Hydrate Equilibrium

Author(s)	Range of T/K	Range of P/MPa	Number of points, N
Roberts et al. (1940)	273.2÷286.7	2.641÷10.804	4
Deaton and Frost (1946)	273.7÷285.9	2.765÷9.784	13
Song et al. (1989)	274.75÷284.4	2.688÷8.099	6
Adisasmito et al. (1991)	273.4÷286.4	2.68÷10.570	11
Deng et al. (1993)	274.9÷284.85	3.0÷9.0	5
Dickens et al. (1994)	276.1÷285.4	3.45÷9.58	7
Hutz et al. (1996)	274.6÷285.35	3.021÷9.350	7
Mei et al. (1996)	274.2÷285.2	2.96÷8.96	12
Nixdorf et al. (1997)	273.49÷284.0	2.716÷7.925	15
Smelik et al. (1997)	273÷284.5	2.482÷8.356	6
Nakamura et al. (2003)	274.25÷284.8	2.92÷8.55	15
Nesterov et al. (2005)	275.15÷300.1	3.17÷54.53	26

The p-T data of the water-hydrate-gas and ice-hydrate-gas three-phase equilibrium in the systems containing pure methane are plotted in Fig. 2-3.

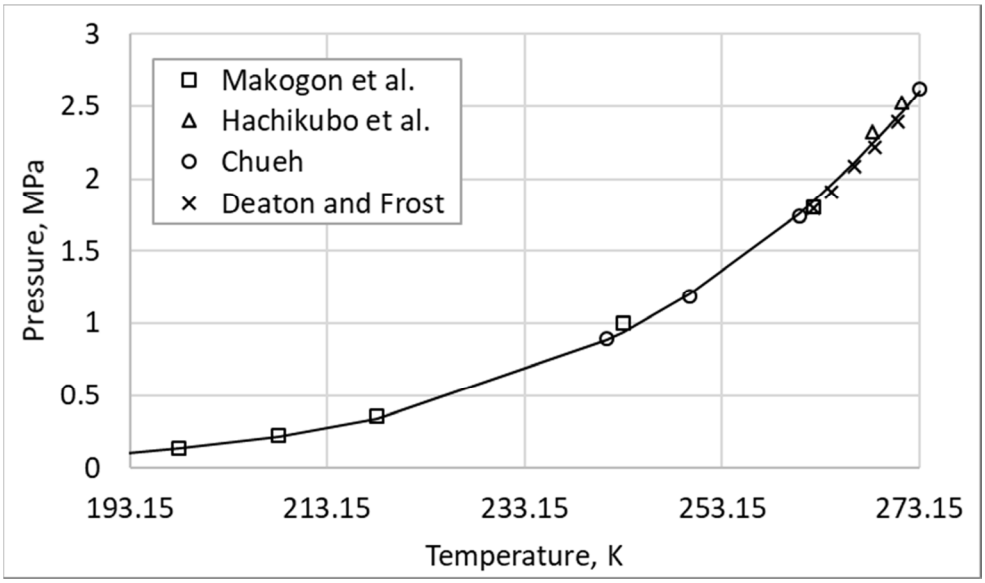

Fig. 2. Literature data on methane-ice-hydrate equilibrium.

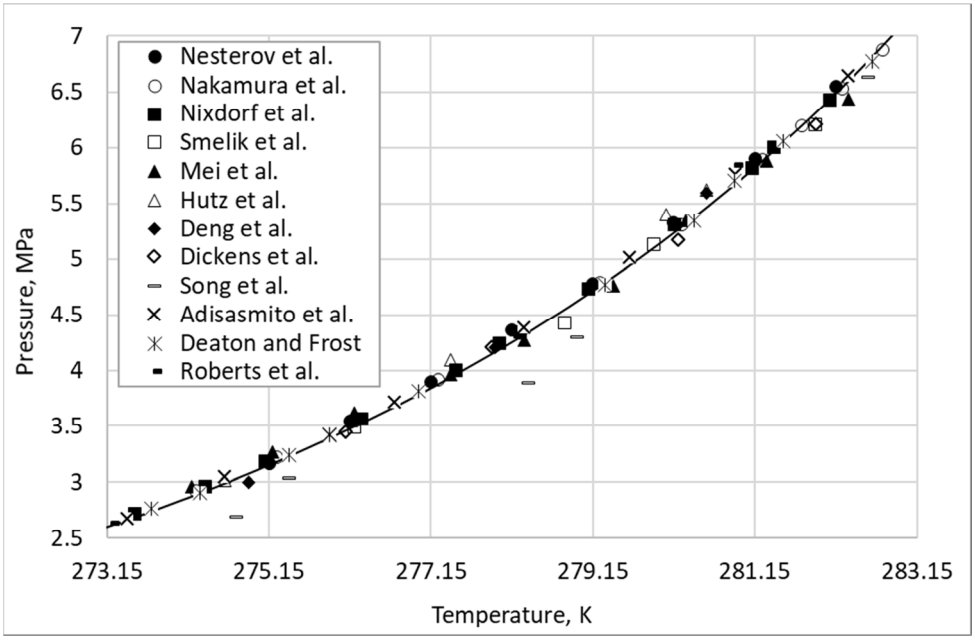

Fig. 3. Literature data on methane-water-hydrate equilibrium.

It is necessary to smooth out the experimental data. Traditionally, pressure dependence on temperature is described by means of empirical function

$$\boldsymbol{ln\, P = A + \frac{B}{T} + C \cdot ln\, T.} \qquad (6)$$

This dependence describes well the equilibrium curves in a larger temperature range and is used to obtain significant thermodynamic information (enthalpy characteristics and hydrate number $\boldsymbol{n}$).

To find the hydrate number (4) and heat of hydration near 273.15 K, it is necessary to approximate the data (Table II and Table III) using the dependence (6). Using all literature data, hydrate number is obtained $\boldsymbol{n}$ = 8.12.

There is a thermodynamic inconsistency of the experimental data; there is no agreement with the data on the

degrees of filling (Table I). According to the data on the degrees of filling, n is approximately 6÷6.5. We conclude that the derivatives are not calculated correctly (the slopes of the lines near 273.15 K are not determined reliably) and it is necessary to smooth the data differently.

The unreliable portion of the data is around 273.15 K. We analyze the experimental data and discard the coarse points that deviate from the averaged values on ≥5%, these data apparently contain systematic errors. Now, according to the available data, we are trying to find the hydrate number.

How to consider derivatives correctly? The working hypothesis is that near 273.15 K we have inaccuracies in the experimental data, which may be due to the effects of ice prefusion, water supercooling, and the speed of the experiment.

C. A new method for correct smooth the experimental data and their correct interpolation

We take into account that the degree of filling in methane is close to one, so $C_1 f \gg 1, C_2 f \gg 1$ can be considered. This assumption can be used for the consistency method. We neglect the unit in the system (5) and find the coordinates m for methane, in which the left and right branches should lie on one curve without a break (Fig. 4).

From equation (5) considering ($C_1 f \gg 1, C_2 f \gg 1$) one can obtain

$$\boldsymbol{m = ln\, f\,(T) + \frac{23}{4RT}\Delta V_{hi}(P - P_0),} \qquad \boldsymbol{T < 273.15\ K,} \tag{7.a}$$

$$\boldsymbol{m = ln\, f(T) + + \frac{23}{4RT}\left(\Delta \mu^0_{wi}(T) + \Delta V_{wh}(P - P_0) + RT\, ln(1 - x)\right),} \qquad \boldsymbol{T \geq 273.15\ K.} \tag{7.b}$$

Fig. 4 illustrates that all experimental data points lie on one curve without a break. After that, we find new smoothed meanings for pressure and temperature, and calculate hydrate number.

Fig. 5 shows two variants of the curves that were obtained by processing the experimental data in two different ways.

Using the proposed method, we obtain intersection of the curves of methane-ice-hydrate and methane-water-hydrate at 273.15 K, and a more correct slope of the curves near this point, a hydrate number $\boldsymbol{n}$ = 6.32 that satisfies the notions of the structure of the hydrate lattice and the degrees of methane filling $\boldsymbol{n}$ between 6 and 6.5.

So, the new data processing method, which allows checking the thermodynamic consistency of the experimental data and their correct interpolation, was provided. This method allows to identify areas where experimental data are unreliable and to smooth them. Smoothed data can give correct values of the enthalpy of decomposition of hydrates to ice and water, a correct value of the quadrupole point, a hydrate number at the quadrupole point.

IV. CONCLUSIONS

Experimental data on three-phase equilibria of methane hydrate were analyzed in detail. It was established that the experiments are not reliable near 273 K and at the temperature range 260-270 K. The new method of thermodynamic consistency and checking of the experimental data was proposed. The method is based on some simplification of Van-der-Waals–Platteeuw and Barrer-Stuart statistical thermodynamic model for gas hydrates as non-stoichiometric ideal solid solutions.

So the smoothed reference data of the equilibria "methane – ice – methane hydrate" and "methane – liquid water – methane hydrate" were obtained. By using the smoothed equilibrium data, the correct calculations of hydrate decomposition enthalpies to ice and to liquid water as well as hydrate number at the quadruple point were presented. The obtained hydrate number n for methane hydrate is in good agreement with direct spectroscopic (NMR and Raman spectroscopy) methods. The proposed method may be applied to other hydrate-forming gases, especially for the gases when in hydrate structures the small cavities are not filled (i.e., ethane, propane, cyclo-propane, isobutane hydrates) and when both small and large cavities are practically completely filled (inert gases, nitrogen, hydrogen sulfide, oxygen hydrates).

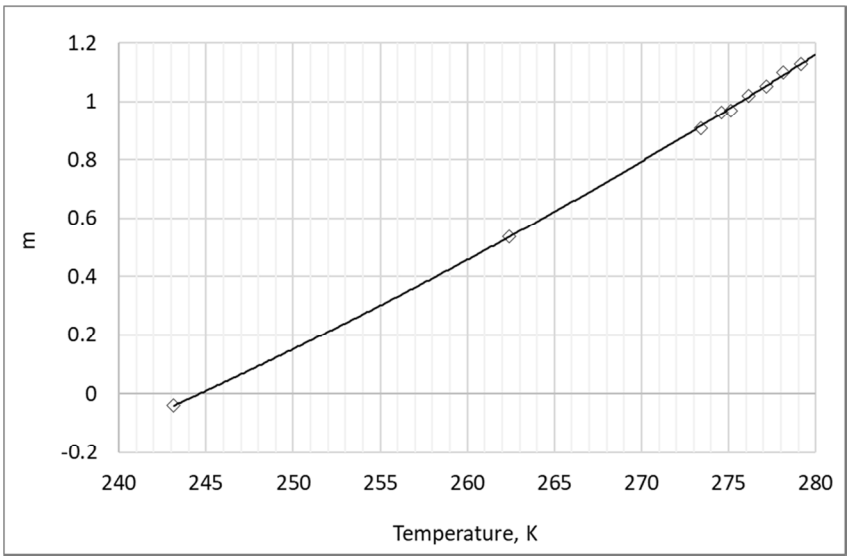

Fig. 4. Experimental data (three-phase equilibrium of the gas-water (ice)-hydrate system) in coordinates m and T.

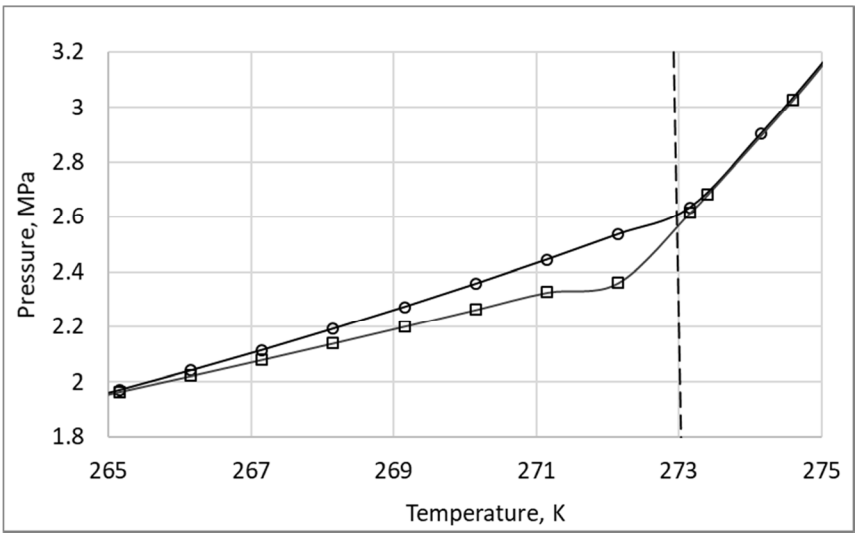

Fig. 5. Three-phase equilibrium of the gas-water (ice)-hydrate system. Pseudo experimental data. □- using (6), ○- using (7.a, 7.b).

V. REFERENCES

[1] V. Istomin, "Prevention and Liquidation of Gas Hydrates in Gas and Oil Systems", 1990, VNIIGAZ, Moscow, 214 pp., the first edition (in Russian).

[2] D. W. Davidson, Y. P. Handa, C. I. Ratcliffe, J. A. Ripmeester, J. S. Tse, J. E. Dahn, F. Lee, L. D. Calvert, Crystallographic studies of clathrate hydrate, 1986, Part I: - Mol.Cryst.Liq.Cryst, v. 141, pp. 141–149.

[3] V. A. Istomin, V. G. Kvon, The prevention and Liquidation of gas hydrates in of gas production systems Moscow, IRTs Gazprom, 2004, 506 pp., the second edition (in Russian).

[4] T. J. Galloway, W. Ruska, P. S. Chappelear, R. Kobayashi, Experimental Measurement of Hydrate Numbers for Methane and Ethane and Comparison with Theoretical Values, 1970, Ind. Engng. Chem. Fundam, v. 9, pp. 237–243.

[5] J. L. De Roo, C. J. Peters, R. N. Lichtenthaler, G. A. M. Diepen, Occurrence of methane hydrate insaturated and unsaturated solutions of sodium chloride and water in dependence of temperature and pressure, 1983, American Institute of Chemical Engineers Journal, v. 29, pp. 651–657.

[6] Y. P. Handa, J. S. Tse, Thermodynamic properties of empty lattices of structure I and structure II clathrate hydrates, 1986, J. Phys. Chem., v. 90 (22), pp. 5917–5921.

[7] J. A. Ripmeester, C. I. Ratcliffe, Low-temperature cross-polarization/ magic angle spinning carbon-13 NMR of solid methane hydrates: structure, cage occupancy, and hydration number, 1988, J. Phys. Chem., v. 92 (2), pp. 337–339.

[8] O. L. Roberts, E. R. Brownscombe, L. S. Howe, Constitution diagrams and composition of methane and ethane hydrates, 1940, Oil & Gas J., v. 39(30), pp. 37–43.

[9] W. M. Deaton, E. M. Frost, Gas hydrates and their relation to the operation of natural-gas pipe lines, 1946, United States Department of the Interior Gas Hydrates and Their Relation to the Operation of Natural-Gas Pipe Lines, U18401 8653273.

[10] D. N. Glew, Aqueous solubility and the gas hydrate the methane-water system, 1962, J. Phys. Chem., v. 66, p. 605.

[11] P. L. Chueh, Arctic pipeline natural gas water content, 1973, [Online]. Available: https://gashydrates.nist.gov/HydrateViewer/.

[12] B. J. Falabella, A Study of Natural Gas Hydrates, 1975, Ph.D. Chemical Engineering Dissertation, University of Massachusetts.

[13] T. Y. Makogon, E. D. Sloan, Phase Equilibrium for Methane Hydrate from 190 to 262 K, 1994, J. Chem. Eng. Data, v. 39, pp. 351–353.

[14] A. Hachikubo, A. Miyamoto, K. Hyakutake, K. Abe, H. Shoji, Phase Equilibrium Studies on Gas Hydrates Formed from Various Guest Molecules and Powder Ice, 2002, The Fourth International Conference on Gas Hydrates, Yokohama, Japan, 19-23, pp. 357–360.

[15] K. Y. Song, R. Kobayashi, Final hydrate stability conditions of a methane and propane mixture in the presence of pure water and aqueous solutions of methanol and ethylene glycol, 1989, Fluid Phase Equilib, v. 47, p. 295.

[16] S. Adisasmito, R. J. Frank, E. D. Sloan, Hydrates of Carbon Dioxide and Methane Mixtures, 1991, J. Chem. Eng. Data, v. 36(1), pp. 68–71.

[17] Y. Deng, X. Xu, L. Zhang, A Primary Study on Composition of Methane Hydrate, 1993, Permafrost Sixth International Conference, Beijing, China, July 5–9.

[18] G. Dickens, M. Quinby-Hunt, Methane hydrate stability in seawater, 1994, Geophysical Research Letters, v. 21(19), pp. 2115–2118.

[19] U. Hutz, P. Englezos, Measurement of Structure H Hydrate Phase Equilibrium and the Effect of Electrolytes, 1996, Fluid Phase Equilib, v. 117, pp. 178–185.

[20] D. Mei, J. Liao, J. T. Yang, T. M. Guo, Experimental and Modeling Studies on the Hydrate Formation of a Methane + Nitrogen Gas Mixture in the Presence of Aqueous Electrolyte Solutions, November 1996, Ind Eng Chem Res., v. 35(11), pp. 4342–4347.

[21] J. Nixdorf, L. R. Oellrich, Experimental determination of hydrate equilibrium conditions for pure gases, binary and ternary mixtures and natural gases, 1997, Fluid Phase Equilib., v. 139, pp. 325–333.

[22] E. Smelik, H. E. King Crystal-growth studies of natural gas clathrate hydrates using a pressurized optical cell, 1997, American Mineralogist, v. 82, pp. 88–98.

[23] T. Nakamura, T. Makino, T. Sugahara, K. Ohgaki, Stability boundaries of gas hydrates helped by methane - structure-H hydrates of methylcyclohexane and cis-1,2-dimethylcyclohexane, 2003, Chem. Eng. Sci., v. 58, pp. 269–273.

[24] P. Gayeta, C. Dicharrya, G. Mariona, A. Graciaaa, J. Lachaisea, A. Nesterovb. Experimental determination of methane hydrate dissociation curve up to 55MPa by using a small amount of surfactant as hydrate promoter, 2005, Chem. Eng. Sci., v. 60, pp. 5751–5758.

Focus

Analysis of interdependencies between Gas and Electric Power systems for optimal dispatching and reliability assessment

A. Churkin

Abstract -This paper analyzes existing studies of gas and electricity systems interconnections. The number of such studies has significantly increased over the last decade due to expansion of both electric power and gas systems and widespread use of gas-fired power plants. However, examination of gas/electricity correlations appears to be a rather complex task with various possible solutions. Some studies examine typical schemes with a moderate number of nodes and analyze optimal dispatching and gas pressure control. Others perform global optimization on a scale of a certain country or even interstate power exchange. Although each study has its own particular goal, the basic principles of the systems interconnections remain the same. The main techniques and approaches to modeling of gas/electricity interdependencies are reviewed in this paper. Proposals for future research are also made.

Index Terms - gas network, electric network, optimal power flow, optimal dispatching, interconnection of systems

I. Introduction

Continious increase of power demand leads to expansion of both electric power and gas systems. Simultaneously, economic and environmental factors encourage usage of gas-fired power plants. Hence, interdependencies between gas and power systems become more obvious. Numerous studies performed in the last decade have shown complexity and multifacetedness of modeling interdependencies.

Most of the existing studies have been performed in the developed countries with wide and complex gas and power systems (UK, Switzerland, US). Such studies [1]-[3] are focused on problems of global dispatching and optimization on a country scale. Main results of the studies show possible reduction in systems operation cost and possible benefits for social welfare.

Another important problem that appears when the two systems are considered together is reliability assessment. In [4] contingency analysis is performed in order to estimate an impact on electric power system and ensure global security. Considering gas system security constraints and gas pressure maintenance, several coordination scenarios among gas and power systems are suggested in [5].

The coupling of gas/electricity concept called "energy hub" is presented in [6]-[8]. Different power flows are considered interconnected in "hubs" in order to get operational and economic benefits. The concept decomposes optimal power flow problem into subproblems that could be effectively solved for each "hub". Gas and electricity interdependencies have also been studied on the interstate scale. Model suggested in [9] performs cross-border energy trade optimization for the European Union countries.

Rather innovative methodology described in [10] estimates operational impact of Power-to-Gas (P2G) technology on electrical and gas transmission networks. This technology enables to convert excessive electric energy into synthetic gas that could be stored in gas transmission network. P2G technology can be considered as inverse coupling of the two systems that extend dispatching and optimization horizons.

Finally, the possibility of demand-side response in combined gas and electricity networks is studied in [11]. It can enhance power system flexibility and reduce investments in further systems development.

Although each study is focused on a particular problem that exists at the confluence of the two systems, the

A. I. Churkin is with the Center for Energy Systems, Skolkovo Institute of Science and Technology, Skolkovo Innovation Center, Building 3, Moscow 143026, Russia (e-mail: andrey.churkin@skolkovotech.ru).

basic principles of the systems interconnections remain the same. This article analyzes basic principles of modeling gas/electricity interdependencies and suggests direction for further research. In section II, the main concept of gas and electricity systems interconnection is presented as well as possible ways of global optimization. Section III provides methodology for gas and electricity systems modeling. Section IV summarizes the main points of the paper.

II. Basic concept

Despite different goals of modeling mentioned above the basic principle of modeling gas/electricity interdependencies can be inferred: gas-fired power plants are considered as the main linkage between the two systems (Fig. 1). For example, in order to produce a certain amount of electric energy, a generator must consume a certain volume of gas. Gas compressor can also be considered as an interconnection point since it consumes electric energy in order to maintain gas pressure. Together with P2G technology, gas compressors form inverse coupling of the two systems. However, such inverse coupling can be neglected in comparison to the power produced by gas-fired generators.

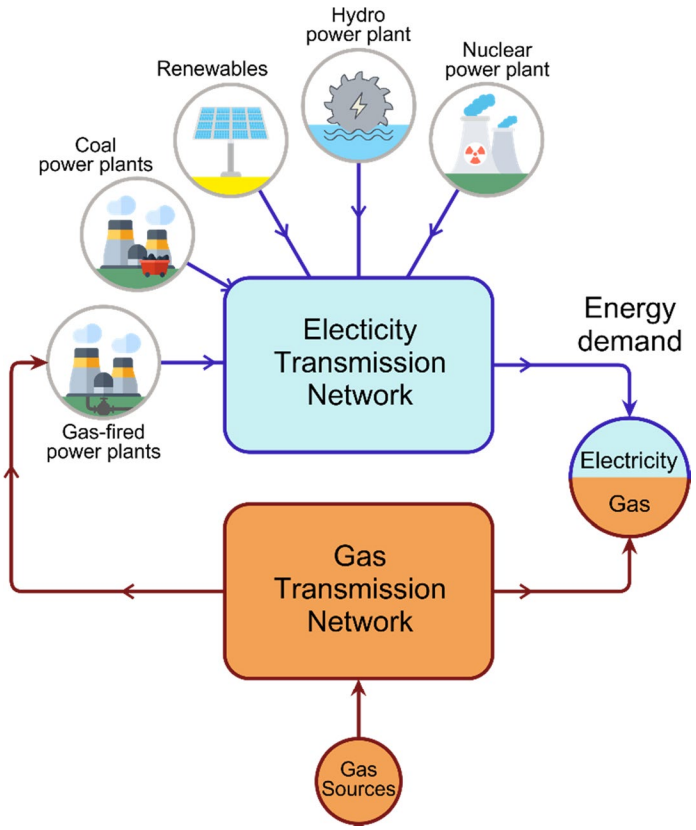

Fig. 1. Gas-fired power plants as main interconnection points between gas and electric power networks.

Thus, power can be transmitted to users in two ways: through electricity transmission network or mostly by gas transmission network (in form of gas) with further conversion into electricity. Both gas and power networks have been well studied individually. It is well known how to perform optimal power flow optimization for power systems as well as gas flow optimization and compressors scheduling [5]. The question arises, what economic benefits can be obtained in case of global optimization and dispatching (gas + power optimal flow). Solution to this problem becomes a sophisticated mathematical and engineering task since we complicate an objective function, add more restrictions and variables (generators output capacity and power of gas compressors).

Before approaching this task, the main modeling methodologies for gas and power systems modeling should be analyzed. The review of existing methodologies is presented in the next section.

III. Modeling methodology

A. Power network modeling

There limited options regarding modeling methodology for power network. Most of the listed studies [2], [3], [5], [9] successfully use direct current (DC) approximation for electric power system states modeling. DC power flow formulation enables the calculation of power flows in each particular transmission line in case when there is a lack of precise data about existing power networks.

Modeling formulations are rather obvious and require Kirchoff's laws implementation, and constraints satisfaction.

Total system power constraint:

$$\sum_{\boldsymbol{\nu}} \big(\boldsymbol{p_i(t)} - \boldsymbol{h_i(t)}\big) = \mathbf{0}, \qquad (1)$$

where $p_i(t)$ is production profile of generator i; $h_i(t)$ is consumption profile of load i; ν – total number of nodes.

Generator production limit:

$$\boldsymbol{p_i^{min}} \leq \boldsymbol{p_i(t)} \leq \boldsymbol{p_i^{max}}. \qquad (2)$$

Power flow limits:

$$-\boldsymbol{f_{ij}^{max}} \leq \boldsymbol{M_{ij}}\big(\boldsymbol{p(t)} - \boldsymbol{h(t)}\big) \leq \boldsymbol{f_{ij}^{max}}, \qquad (3)$$

where f_{ij}^{max} is power flow limit of a certain transmission line; matrix M represents correspondence between line power flows and power injections at nodes.

Thus, power network modeling is usually performed for steady-state conditions within a single time-step (taken as 1 hour). In order to model system behavior for the period of one day, $T = 24$ power states have to be calculated. If gas system modeling is performed dynamically, values for power system must be converted to continuous values also. This can be done as following integration:

$$\boldsymbol{min} \quad \boldsymbol{J_p} = \sum_{\boldsymbol{i \in \nu}} \int_{\mathbf{0}}^{\boldsymbol{T}} \big[\boldsymbol{c_i} \cdot \boldsymbol{p_i(t)} + \boldsymbol{c_k} \cdot \boldsymbol{\Delta p_k(t)}\big]\, \boldsymbol{dt}, \qquad (4)$$

where J_p is an objective function that minimizes total cost of generation and cost of power losses; c_i represents cost functions of production; c_k represents cost of power losses $\Delta p_k(t)$ in transmission lines.

B. Gas network modeling

Gas network modeling is not as clear as power network modeling. The main challenge is physics of gas flow. Gas flows much slower than electricity. This means that gas dynamics cannot be easily neglected. There are some approaches of steady-state gas network modeling, but they are rather rough and inaccurate. Hence, existing studies are divided into gas steady-state modeling approaches and dynamic modeling approaches. Moreover, each study suggests its own gas flow equations and objective function representations. Such variety of methods makes it extremely hard to find the best optimization solution for the gas and power systems coupling.

Another difficulty of gas network modeling is presentation of such gas equipment as compressors and gas storages. These two essential components of gas network can also be modeled in different ways. Gas compressors can be presented as a function that changes pressure at a node where it is installed. Gas storages can be presented as gas injections into network.

Thus, there are different approaches and equations for modeling gas flows in gas pipelines, gas compressors and storages. We will focus only on the meaning of the equations, not describing numerous physical formulas. More detailed information about the modeling can be found in [1], [2], [3], [5].

Each gas flow (φ_{ij}) can be represented as function dependent on pressure difference ($\rho_i - \rho_j$) between ends of a pipeline or as a system of differential equations that involves gas pressure (ρ), friction factor (λ) and many other parameters.

$$\boldsymbol{\varphi_{ij} = f\left((\rho_i - \rho_j), \lambda, \dots\right).} \quad (5)$$

Gas modeling constraints include nodal balance condition (6), gas pressure values constraints (7), power of compressor (CP_i) constraint (8), compressor ratio (θ_i) constraint (9), withdrawal from gas storage constraint (10) and gas pipeline limits (11).

$$\sum_{i \in N} \varphi_{ij} + \sum_{i \in N} I_i - \sum_{i \in N} d_i = 0, \quad (6)$$

where I_i is gas injection to a certain node i; d_i stands for gas demand at a node; N – total number of nodes in gas network.

$$\rho_i^{min} \le \rho_i(t) \le \rho_i^{max} \quad (7)$$

$$CP_i \le CP_i^{max} \quad (8)$$

$$\theta_i^{min} \le \theta_i \le \theta_i^{max} \quad (9)$$

$$I_i \le I_i^{max} \quad (10)$$

$$\varphi_{ij}^{min} \le \varphi_{ij}(t) \le \varphi_{ij}^{max}. \quad (11)$$

C. Gas and electricity optimal power flow

Global optimization involves objective functions and restrictions of both gas and electric power systems. One of the possible optimization problems can be stated as total operation cost minimization. This means reduction of power losses along with low cost power generation and optimal scheduling of compressors. An objective function for this case will be:

$$J_{pg} = \int_0^T \left[\sum_{i \in v} \{c_i \cdot p_i(t) + c_k \cdot \Delta p_k(t)\} + \sum_{i \in N} c_e \cdot CP_i(t) \right] dt, \quad (12)$$

where c_e represents cost of compressors operation.

Thus, the minimization problem is:

$$\min_{p_i(t), \theta_i} \quad J_{pg}$$

subject to: power system constraints (1-3)

gas system constraints (6-11) (13)

Result of the optimization will show the new optimal regimes of gas and power systems that will be the most beneficial for society. Applying of gas flow differential equations will also enable gas pressure control over time [5].

IV. Conclusion

Analysis of interdependencies between gas and electric power systems extends boundaries of optimal operation and dispatching and poses new complex problems that can be treated in several ways. On the one hand, objective function can be aimed at security maintenance or reduction of operation cost, while on the other hand, there is a variety of modeling methodologies that can be implemented.

However, in spite of scientific novelty, practical application of the research in the direction of gas and power systems coupling is rather obscure. The main obstacle is that application of global dispatching and optimization

needs significant technical and regulatory development. Therefore, in order to attract attention of government and transmission system operator, a real case should be studied and optimized. It will show what benefits could be obtained. Furthermore, it is not clear yet how these benefits should be shared among all participants of the optimization (system operator, power grid company, generating companies and gas companies). Each participant has to be motivated to contribute to the optimization.

Global reliability assessment can also be performed for the coupled systems. Since each particular gas-fired power plant has an emergency fuel reserve (oil), only serious long-term incidents should be considered in contingency analysis. The mentioned pressure maintenance methodologies should be also verified for real systems.

In summary, existing approaches of the coupled modeling and optimization have to be verified for real cases. First of all, values of total benefits should be calculated and announced in order to attract industry partners and attention of the government. Then, distribution of total benefits should be suggested.

Further work will be focused on a real case examination.

V. References

[1] S. An, Q. Li, T.W. Gedra, "Natural gas and electricity optimal power flow," Transmission and Distribution Conference and Exposition, 2003 IEEE Power Engineering Society, vol. 1, 7–12, pp. 138–143, 2003.

[2] C. Unisihuay, J.W. M. Lima, and A.C.Z. de Souza, "Modeling the Integrated Natural Gas and Electricity Optimal Power Flow," IEEE Power Engineering Society General Meeting, Tampa, Florida, June 24–28, 2007.

[3] M. Chaudry, N. Jenkins, G. Strbac "Multi-time period combined gas and electricity network optimization," Elec. Power Syst. Research, Vol. 78, No.7, pp. 1265–1279, 2008.

[4] Shahidehpour, M., Fu, Y., Wiedman, T., "Impact of natural gas infrastructure on electric power systems," Proceeding of the IEEE 93 (5): 1042–1056, 2005.

[5] A. Zlotnik, L. Roald, S. Backhaus, M. Chertkov, G. Andersson, "Coordinated Scheduling for Interdependent Electric Power and Natural Gas Infrastructures," IEEE Transactions on Power Systems, vol. 32, no. 1, pp. 600–610, Jan. 2017.

[6] M. Arnold, G. Andersson, "Decomposed electricity and natural gas optimal power flow, " presented at the 16th Power Systems Computation Conference (PSCC 08), Glasgow, Scotland, 2008.

[7] M.Geild, G. Andersson, "Optimal power flow of multiple energy carriers," IEEE Transactions on power systems 22 (1), pp. 145–155, 2007.

[8] A. Hajimiragha, C. Canizares, M. Fowler, M. Geidl, G. Andersson "Optimal energy flow of integrated energy systems with hydrogen economy considerations," Proceedings of Bulk Power System Dynamics and Control – VII, Charleston, SC, USA, Aug. 2007.

[9] C. Spataru, J. W. Bialek, "Energy Networks: a Modelling Framework for European Optimal Cross-Border Trades," PES General Meeting | Conference & Exposition, 2014 IEEE, Oct. 2014.

[10] S. Clegg and P. Mancarella, "Integrated Modeling and Assessment of the Operational Impact of Power-to-Gas (P2G) on Electrical and Gas Transmission Networks," IEEE transactions on sustainable energy, vol. 6, no. 4, pp. 1234–1244, October 2015.

[11] M. Qadrdan, M. Cheng, J. Wu, N. Jenkins, "Benefits of demand-side response in combined gas and electricity networks," Applied Energy 192 , pp. 360–369, 2016.

Skoltech

Skolkovo Institute of Science and Technology

Skolkovo Institute of Science and Technology
Skolkovo Innovation Center, Building 3
www.skoltech.ru/en